Case Studies in Construction Materials 15 (2021) e00746

Contents lists available at ScienceDirect

Case Studies in Construction Materials

journal homepage: www.elsevier.com/locate/cscm

Effects of tension stiffening and shrinkage on the flexural behavior of reinforced UHPFRC beams

Eduardo J. Mezquida-Alcaraz *, Juan Navarro-Gregori, José R. Martí-Vargas, Pedro Serna-Ros

Instituto de Ciencia y Tecnología del Hormigón (ICITECH), Universitat Politècnica de València, Camino de Vera s/n, 46022 València, Spain

ARTICLE INFO

Keywords:
Ultra-high-performance fiber-reinforced concrete
Beams
Finite element modeling
Four-point bending test
Experimental program
Tensile parameters

ABSTRACT

This paper presents a study on the flexural behavior of Ultra-High-Performance Fiber-Reinforced Concrete (UHPFRC) beams, which included conventional reinforcing bars. The study focuses on critical design aspects, such as concrete shrinkage and cracking implications on the tension-stiffening phenomenon. An experimental program with two different sized flexural reinforced UHPFRC beams was run. Beams were cast and tested in a four-point bending test (4PBT) using UHPFRC with different amounts of fibers: 130 and 160 kg/m^3 (1.66% and 2.00% in vol.) to cover a wide range of strain-softening and strain-hardening constitutive UHPFRC behaviors. A non-linear finite element model (NLFEM) was developed to validate the mechanical tensile characterization of UHPFRC when applied to reinforced elements. Both shrinkage and tension-stiffening effects were considered to improve the model. After the NLFEM simulation, very reliable results were obtained at both the service and ultimate load levels compared to the experimental ones. Finally, some aspects about the design of reinforced UHPFRC cross-sections under bending forces are addressed and satisfactorily compared to the experimental results.

1. Introduction and objectives

Ultra-high-performance fiber-reinforced concrete (UHPFRC) can be considered an advanced modernization of conventional (CC) and fiber-reinforced (FRC) concretes. It integrates specialized knowledge about its dosage and high technology to be produced and poured, which can strongly influence its mechanical properties and structural response. A very dense microstructure, given its low water/binder ratio (w/b below 0.25), fine-grained mix and adequate high-strength steel fiber content, leads to compressive strength above 150 MPa, tensile strength higher than 7 MPa and flexural strength between 15 and 40 MPa. All these advantages allow slender lightweight structures compared to conventional reinforced concrete constructions. However, due to the high cement content (about 800 kg/m^3) and its mix design, UHPFRC can be prone to suffer high shrinkage at early ages. Therefore, slender UHPFRC structures can be vulnerable to shrinkage cracking in the manufacturing stage [1–5].

UHPFRC can be considered an expensive material, but can provide a longer service life given its low maintenance requirements and good durability. When UHPFRC structures are efficiently designed, they become considerably cost-effective compared to CC, and even to steel ones. UHPFRC is being studied experimentally and analytically and numerically modeled as either a constituent material or a strengthening component in elements like: shear walls [6,7]; slabs and plates [8–12]; columns [13–15]. With beams, studies have been

* Corresponding author.
E-mail address: edmezal@alumni.upv.es (E.J. Mezquida-Alcaraz).

https://doi.org/10.1016/j.cscm.2021.e00746
Received 10 July 2021; Received in revised form 5 October 2021; Accepted 14 October 2021
Available online 18 October 2021

Nomenclature

UHPFRC	ultra-high-performance fiber-reinforced concrete
SH	strain-hardening
SS	strain-softening
SH-UHPFRC	strain-hardening ultra-high-performance fiber-reinforced concrete
SS-UHPFRC	strain-softening ultra-high-performance fiber-reinforced concrete
4PBT	four-point bending test
NLFEM	non-linear finite element model
CC	conventional concrete
RC	reinforced concrete
FRC	fiber-reinforced concrete
RPC	reactive powder concrete
HPFRCC	high-performance fiber-reinforced cement composites
4P-IA	simplified four point inverse analysis
JE-1	long reinforced beam with 20 mm diameter of reinforcement bars
JE-2	long reinforced beam with 16 mm diameter of reinforcement bars
XS1	UHPFRC's basic dosage with 160 kg/m^3 of steel fibers
XS2	UHPFRC's basic dosage with 130 kg/m^3 of steel fibers
P	Penetron crystalline admixtures
ANF	alumina nanofibers
CNC	cellulose nanocrystals
CNF	cellulose nanofibrils
C.V.	coefficient of variation

List of symbols

P	load
σ or σ_{fl}	equivalent bending stress
δ	deflection
L	specimen length
b	specimen width
h	specimen height
ϕ	reinforcement bar diameter
E	elastic modulus
E_s	elastic modulus of reinforcement steel
f_{st}	tensile strength of reinforcement steel
f_{stu}	ultimate tensile strength of reinforcement steel
f_t	tensile strength
f_{tu}	ultimate tensile strength obtained from the 4P-IA previous the softening correction application
f_{tuc}	corrected ultimate tensile strength
γ	hardening ratio: quotient between ultimate tensile strength (f_{tu}) and tensile strength (f_t)
γ_c	corrected hardening ratio: quotient between corrected ultimate tensile strength (f_{tuc}) and tensile strength (f_t)
$\varepsilon_{st,el}$	elastic strain of reinforcement steel
$\varepsilon_{st,u}$	ultimate tensile strain of reinforcement steel
ε_{tu}	ultimate cracking strain
ε_{comp}	average strain at the mid-span section at the compression displacement transducer's height
ε_{tens}	average strain at the mid-span section at the tension displacement transducer's height
w_{ftuc}	crack opening at corrected ultimate tensile strength (f_{tuc})
w_0	crack opening at the intersection that defines the initial slope to the w axis in the σ-w diagram
b_w	material crack bandwidth or process zone
f_c	cubic compression strength
$\varepsilon_{csUHPFRC}$	total shrinkage strain of UHPFRC
ε_{cs}	shrinkage strain obtained on the testing day using Eurocode 2
sh	UHPFRC shrinkage
sh_{inc}	percentage of UHPFRC shrinkage increment
EI_{exp}	experimental flexural stiffness of the section
EI_{cr}	flexural stiffness in the fully cracked section
EI_g	flexural stiffness in the gross (uncracked) section
K	coefficient of orientation
$f_{c,cyl}$	concrete compressive strength obtained in a cylinder

x_0	location of the neutral axis
$M_{u,cal}$	maximum bending moment that the reinforced UHPFRC cross-section can resist
$M_{u,exp}$	maximum bending moment achieved in the test
N_c	axial force on concrete
N_f	axial force on steel fibers
N_s	axial force on longitudinal reinforcement bars
β	tension-stiffening factor
I_e	effective moment of inertia

done about the behavior of reinforced UHPFRC under shear force in different circumstances [16–19]: adapting well, proving theories for CC to UHPFRC such as the Modified Compression Field Theory, and developing experimental programs with UHPFRC and composite beams. Studies on flexural UHPFRC beams [17,20–25] have dealt with experimental large-scale UHPFRC beams by representing the cracking pattern characterized by multiple microcracking in initial stages, followed by the evolution of a macrocrack in a singular section while load increases. The tension-stiffening behavior of reinforced concrete (RC) and FRC is fundamental for the characterization of crack widths and separation. It is directly related to the crack pattern and effects such as shrinkage, and also to the determination of the tensile response of FRC members with bar reinforcement [26–28]. Relevant research into tension-stiffening has been addressed for UHPFRC. To better understand the serviceability behavior of concrete structures, Sturm et al. [29] developed and extended a non-linear tension-stiffening approach to FRC and UHPFRC by considering its particular strain-hardening stress-strain relation prior to macrocracking. Hung et al. [30] suggested a constitutive model capable of reasonably representing the tension-stiffening behavior of UHPFRC up to failure. Tensile responses of steel-reinforced UHPFRC samples were evaluated using multiple performance measures, including damage pattern, stiffness, load-deformation relation, rebar strain and tension-stiffening behavior of UHPFRC. At the same time, the development of numerical models to predict the structural response in bending of UHPFRC elements has emerged from studying the influence of different amounts of steel fibers, the interaction with reinforcement and loading conditions. In this direction, it is important to set out how UHPFRC is mechanically characterized and how this behavior is implemented into the material model. Very accurate solutions for modeling UHPFRC beam specimens on different scales have been obtained by applying the damage plasticity model, where material properties are obtained from cubes and cylinders in compression, and by using uniaxial tensile tests or three-point bending tests with inverse analysis to characterize tensile behavior [21,31–33].

As a result of its evolution, UHPFRC is considered in recommendations, standards and design codes worldwide. In Australia, the recommendations of Ductal® properties [34] provide guidelines to design prestressed concrete beams cast using Ductal's Reactive Powder Concrete (RPC). Recommendations follow the philosophy of the limit state approach according to the design requirements of the Australian Standard for Concrete Structures AS3600–1994 [35]. The Japan Society of Civil Engineering considerations [36] address the design and construction of high-performance fiber-reinforced cement composites (HPFRCC) and steel-reinforced structures. They assume that the design process for HPFRCC structures are based on Standard Specifications for Concrete Structures [37], in which limit states corresponding to each performance requirement are prescribed. These recommendations exclude non reinforced HPFRCC structures. For these cases, they refer to the Standard Specification for Concrete Structures. In the USA, the Federal Highway Administration [38] delivered a report that presents the state of the art for applying UHPFRC on highway transportation infrastructures. For design purposes, it summarizes information available about the structural design of UHPFRC members corresponding mainly to articles in the AASHTO Load & Resistance Factor (LRFD) Bridge Design Specifications [39]. The French standard for UHPFRC [40,41] is related to recommendations [42] and follows the plan of Eurocode 2 [43] for structural design purposes based on a limit state design in conjunction with the partial factor method. The Swiss standard [44] is an adaptation of UHPFRC to the proper national standards for concrete design [45], and is also based on the limit state design. Therefore, it can be concluded from the principal standards and recommendations for UHPFRC structural design that they are practically all adaptations from CC design codes.

The research group has realized that the majority of research that has dealt with UHPFRC in the past 20 years has been related to strain-hardening behavior (SH-UHPFRC). This behavior ensures excellent mechanical properties and durability, but with a high initial cost related to raw materials, pouring system, curing and heat treatment once the UHPFRC is cast. The study of the behavior of UHPFRC with strain-softening (SS-UHPFRC) has been considered to a lesser extent and this could result in the possibility of reducing the use of these raw materials in its manufacture. Is it necessary to produce SH-UHPFRC to obtain excellent properties? Is it possible to develop SS-UHPFRC that leads to lower initial costs and to maintain competitive mechanical and durability properties that result in an effective structural design? The development of, what is considered in the French standard for UHPFRC [40–42], low strain-hardening and SS-UHPFRC would lead to reduce its mechanical properties, but they can be optimized if they are studied and controlled. This would lower the initial UHPFRC cost by, for example, reducing the amount of steel fibers used in its dosage. Therefore, in order to make UHPFRC an efficient and economically competitive material for structural designs and applications a clear and robust definition of material models and their interaction, a suitable numerical technique that allows complex analyses to be performed and an easy-to-run UHPFRC material characterization procedure for both SH and SS-UHPFRC to accurately establish constitutive material parameters for modeling have been addressed in the research group in previous work [46–51].

In this context, the aim of this paper is to study the contribution of reinforcement bars in UHPFRC elements under bending forces by considering the effects of tension-stiffening mechanism and concrete shrinkage in numerical modeling for structural analysis and design. Another intention is to validate the accuracy of traditional design methods for reinforced UHPFRC sections under serviceability and failure conditions. To this end, a method for UHPFRC tensile characterization for numerical modeling and design in both: SH and SS-UHPFRC was set up and validated by a non-linear finite element model (NLFEM). In the following sections, the experimental

Table 1
Reference UHPFRC mix designs (kg/m^3).

kg/m^3	XS1	XS2
CEM I 42.5 R-SR	800	800
Silica Fume	175	175
Water	160	160
w/c	0.200	0.200
w/b	0.164	0.164
Silica sand – 0.8 mm	565	–
Silica sand – 0.4 mm	302	1092
Silica flour	225	–
Short steel fibers (13/0.2)	160	130
Plasticizer Sika 20 HE	30	30

Table 2
Functionalized additives used for UHPFRC.

Id.	Additive
P	Penetron crystalline admixtures
ANF	Alumina Nanofibers
CNC	Cellulose Nanocrystals
CNF	Cellulose Nanofibrils

Table 3
List of functionalized UHPFRCs prepared from XS1 and XS2 basis.

XS1 (160 kg/m^3)	XS2 (130 kg/m^3)
XS1 + 0.8% P	XS2 + 0.8% P
XS1 + 0.8% P + 0.25% ANF	XS2 + 0.8% P + 0.25% ANF
XS1 + 1.6% P + 0.25% ANF	XS2 + 0.8% P + 0.15% CNC
XS1 + 0.15% CNF/CNC - (50% each)	XS2 + 0.8% P + 0.15% CNF/CNC - (50% each)
XS1 + 0.8% P + 0.15% CNC	
XS1 + 0.8% P + 0.15% CNF/CNC - (50% each)	

program and test results, the developed NLFEM, the model application and validation, important aspects dealing with designing reinforced UHPFRC cross-sections under bending forces, and comparisons of predicted and experimental values under serviceability conditions and at failure, are presented.

2. Experimental program and test results

To move toward the structure reality, and to model and design reinforced UHPFRC elements, an experimental program including reinforced concrete beams on different scales was carried out. A set of 36 short beams and two large-scale beams were cast. At the same time, prismatic and cubic specimens were cast and tested to characterize the tensile and compressive behavior of the employed UHPFRC, respectively. All the reinforced concrete beams and specimens were tested 49 days after casting.

The different UHPFRC's dosages used to cast the beams started from the basic dosages XS1 with 160 kg/m^3 of smooth-straight (13/0.20) steel fibers and XS2 with 130 kg/m^3, specified in Table 1. Therefore, to cover a wide range of SS and SH constitutive UHPFRC behaviors and with the aim of varying the mechanical properties of UHPFRC also in a wide range, different combinations of the basic dosages were made with the introduction of functionalized additives described in Table 2, in the proportions expressed in percentages of cement content specified in Table 3. These mixes were developed by the research group in the ReSHEALience Project for Ultra High Durability Concrete [52]. More details of the composition of the additives, the definition of the mixes and analysis of the mechanical properties of these dosages can be found in [53,54]. In this sense, different types of UHPFRC with 160 kg/m^3 and 130 kg/m^3 of steel fibers were used to cast the beams.

2.1. Short beams

Short beams were included in the experimental program to constitute a first step toward applying the model herein developed at a structural level.

These specimens were cast at different UHPFRC dosages (see Table 3) by using two amounts of smooth-straight (13/0.20) steel fibers: 130 kg/m^3 (1.66% in vol.) and 160 kg/m^3 (2.00% in vol.) to cover a wide range of SS and SH constitutive UHPFRC behaviors. Beam dimensions were 750×150×100 mm. Fig. 1 shows the geometry and arrangement of the reinforcement of the developed short beams. As observed, the length of the span between support rollers was 600 mm, the length between load rollers was 150 mm and,

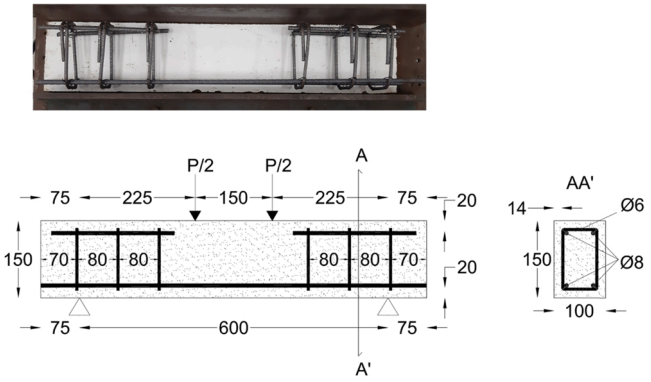

Fig. 1. Geometry (in mm) and reinforcement details of short beams.

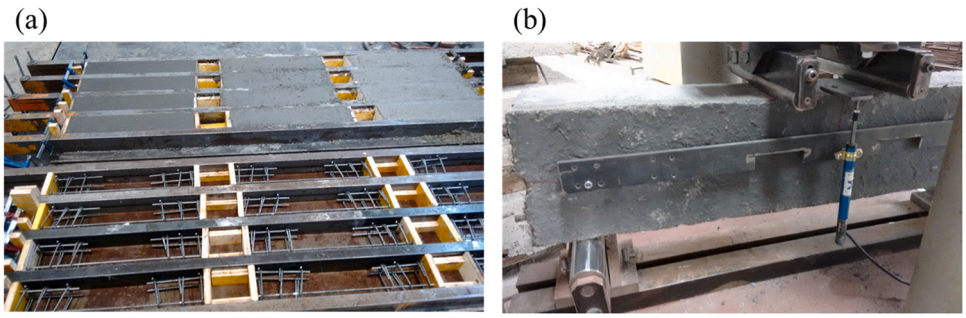

Fig. 2. UHPFRC short beams: (a) overview of the casting zone and (b) the 4PBT setup.

consequently, the shear span between the support and load roller was 225 mm. Regarding reinforcement, six ϕ6 mm B500SD stirrups (three on each end zone of the beam) were symmetrically positioned to allow the development of the bending process by avoiding shear failure; two couples of ϕ8 mm B500SD longitudinal reinforcement bars were placed at the top of the section, one on each side and symmetrically positioned; two ϕ8 mm B500SD longitudinal reinforcement bars were situated at the bottom of the section.

Thirty-six UHPFRC short reinforced beams were cast and tested using a four-point bending test (4PBT) configuration: 13 specimens with 130 kg/m^3 of fibers and 23 with 160 kg/m^3. Fig. 2(a) shows an overview of the casting zone, and Fig. 2(b) depicts the 4PBT setup for these short beams. As observed in Fig. 2(b), one Penny & Giles Controls Ltd displacement transducer was placed to obtain the load-deflection curve at the mid-span. Load was applied by an IBERTEST universal testing machine with a bearing capacity of 1500 kN, measured by a 350 bar/10 V GROBY-PDCR 4011 Druck.

According to Eq. (1) where the experimental load (P) expressed in N is transformed into equivalent stress at the mid-span (σ), a complete stress (σ)-deflection at the mid-span (δ) curve was obtained from each experimental test. Fig. 3 depicts the results of the 4PBT carried out for the 13 reinforced specimens with 130 kg/m^3 of fiber content (Fig. 3(a)) and the 23 with 160 kg/m^3 (Fig. 3(b)).

$$\sigma = 0.0003 \cdot P \quad \left(\mathrm{N/mm^2}\right) \tag{1}$$

As observed in Fig. 3, and regardless of fiber content, curves depict two different stages: a first stage with greater stiffness, where uncracked concrete and reinforcement work together; a second stage with lesser stiffness, where a microcracking process takes place and the tension-stiffening phenomenon develops. In the second stage, microcracks grow in a smeared way by covering part of the span between supports (the so-called process zone) as load increases. When this stage ends, the concentration in one macrocrack takes place. Collapse is imminent at this point. This flexural behavior of UHPFRC is characteristic [1]. Fig. 4 shows one of these short beams after collapse. The developed microcracks and the subsequent concentration in a macrocrack, which generated a very narrow and concentrated compression head, along with the crush in the compression at the top of the section, are observed. Moreover, at collapse, the reinforcement was yielded.

2.2. Long beams

To study large-scale specimens, two long reinforced beams were included in the experimental program. Both beams were cast using XS1 UHPFRC with 160 kg/m^3 (2.00% in vol.) of smooth-straight (13/0.20) steel fibers (see Table 1). Fig. 5 shows the geometry, the arrangement of the reinforcement and the displacement transducer's position of the developed long beams. Dimensions were 4500×300×100 mm (Fig. 5(a)). As shown in Fig. 5(b), reinforcement consisted of two longitudinal bars B500SD of ϕ20 or ϕ16 (ϕ20 for

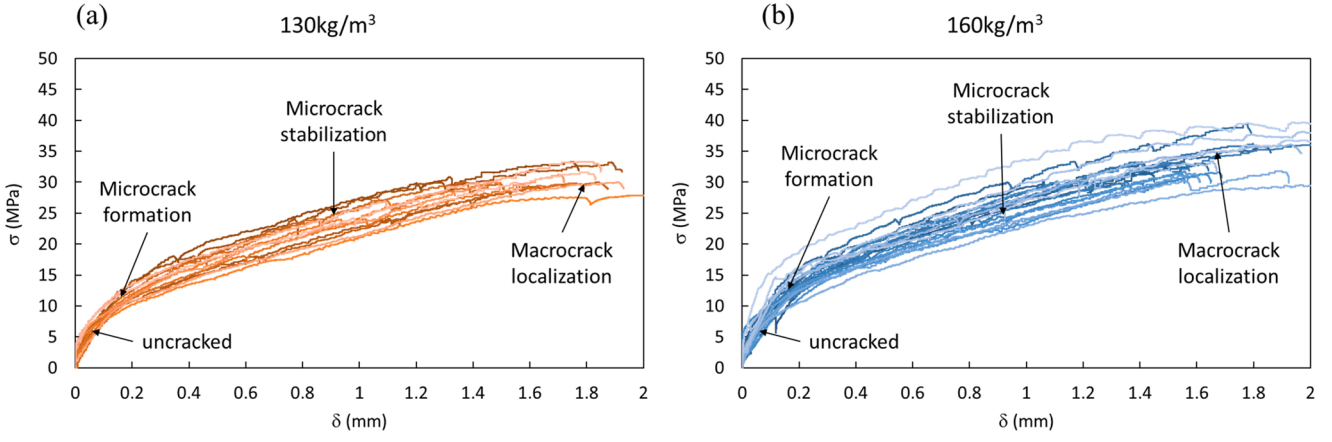

Fig. 3. Experimental 4PBT σ-δ curves for the specimens with (a) 130 and (b) 160 kg/m^3 of fiber contents.

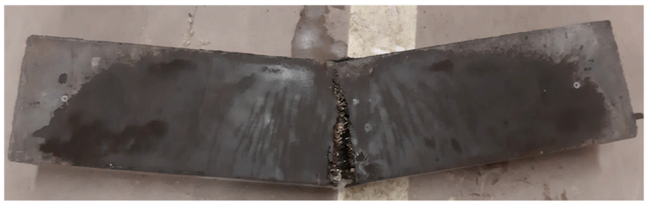

Fig. 4. Collapsed short beam.

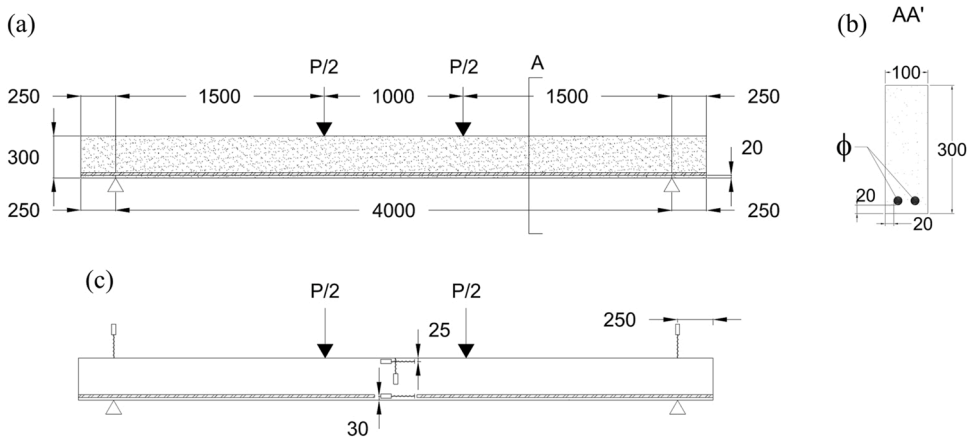

Fig. 5. Long beams: (a) geometry (in mm), (b) reinforcement details and (c) displacement transducer's position.

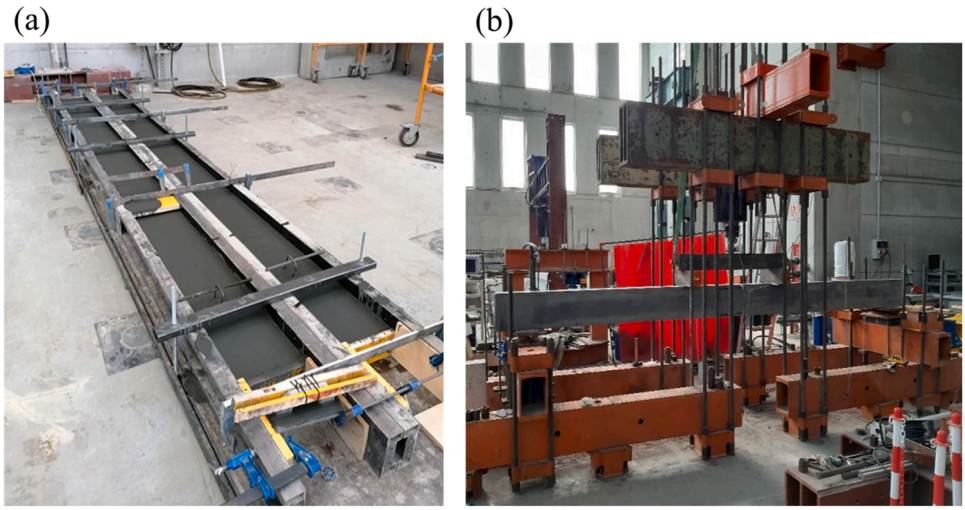

Fig. 6. UHPFRC long beams: (a) overview of the casting zone and (b) testing setup.

one beam (JE-1) and ϕ16 for the other (JE-2)) on the bottom face, with a concrete cover of 20 mm in both cases. Regarding the displacement transducer's position (Fig. 5(c)): two displacement transducers were placed at the mid-span to measure deflection, one on the front face and the other on the back face; two displacement transducers were placed at the support level to register the possibility of vertical displacement there; four displacement transducers (two on the front, two on the back face) in the horizontal position were located at the mid-span at two levels: 25 mm from the top, to measure average compressive strains, and 28 and 30 mm from the bottom (at the reinforcement level), to measure average tensile strains.

Fig. 6(a) shows an overview of the casting zone. Fig. 6(b) depicts the testing setup for the long beams. As observed in Fig. 6(b), the testing load was applied by using a hydraulic jack on an intermediate beam which, in turn, distributed loads on two loading plates, each situated at 1.5 m from the supports, as set out in Fig. 5(a). Fig. 7 shows in detail the intermediate beam and loading plates (Fig. 7 (a)), along with details of the supports' materialization: a sliding support (Fig. 7(b)) and a fixed one (Fig. 7(c)), both including a hinged

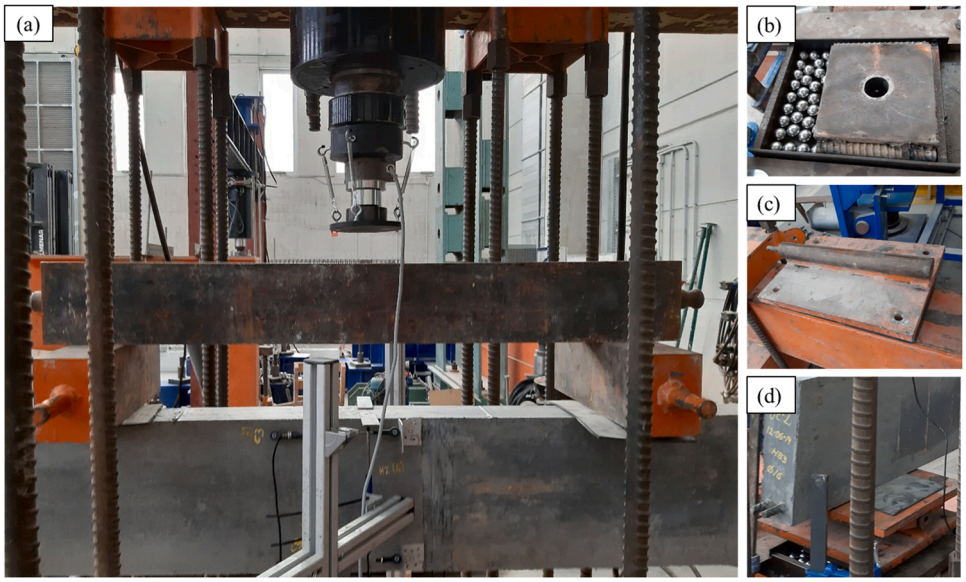

Fig. 7. Testing frame details: (a) intermediate beam and loading plates, (b) sliding support, (c) fixed support and (d) hinged platform.

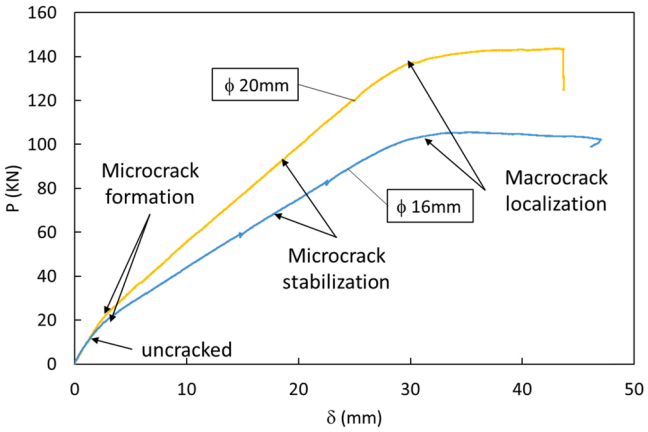

Fig. 8. Load-deflection curve at the mid-span section for beams JE-1 (ϕ20 mm) and JE-2 (ϕ16 mm).

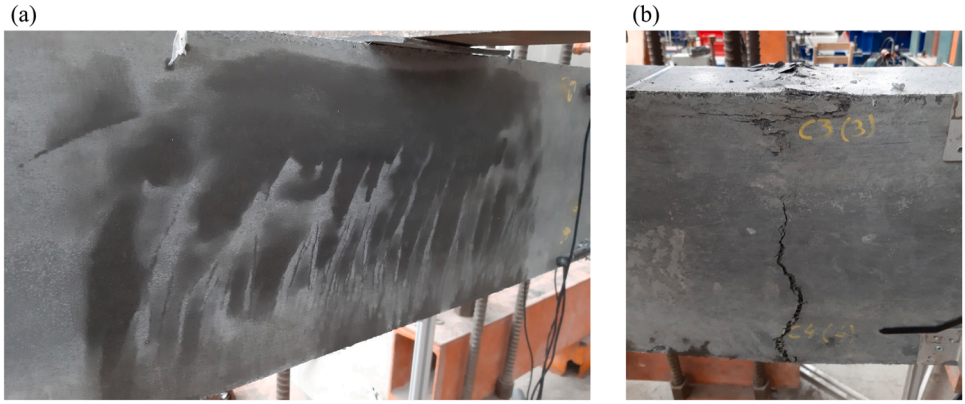

Fig. 9. (a) Microcracking and (b) collapse of a long beam.

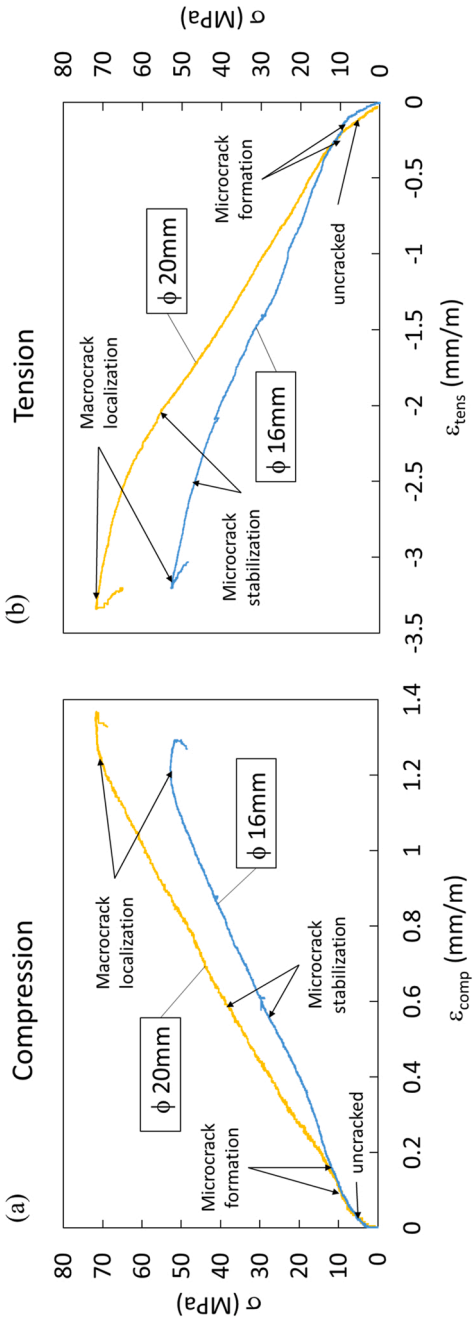

Fig. 10. (a) σ-ε_{comp} curve, (b) σ-ε_{tens} curve.

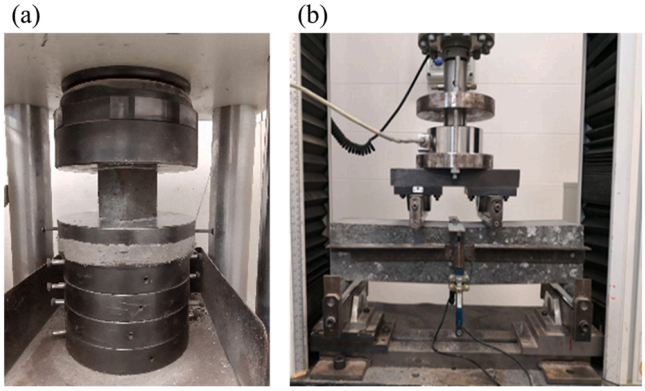

Fig. 11. (a) Compression test and (b) 4PBT.

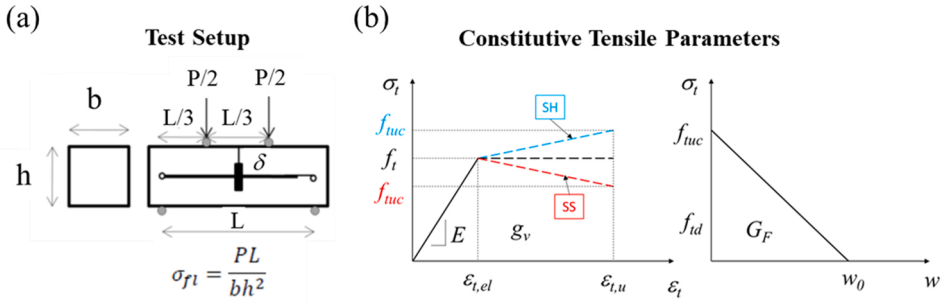

Fig. 12. (a) 4PBT and (b) assumed simplified constitutive tensile law.

platform, were used (Fig. 7(d)). Load was applied under displacement control by a servo-hydraulic HINE actuator with a bearing capacity of 1240 kN (250 mm long). Between the intermediate beam and the actuator a 500 kN HBM-C6A load cell was attached to measure the total load transmitted by the jack (Fig. 7(a)).

For the JE-1 and JE-2 beams, Fig. 8 shows the curves obtained from the experimental measurements taken of the vertical displacement transducers at the mid-span, corrected by the measurements of the supports' displacement transducers.

As in the short beams, the same pattern was developed while testing for the long beams (see Fig. 8). When concrete reached its tensile strength, a microcracking phase took place and the tension-stiffening phenomenon develops (see Fig. 9(a)). Afterward, a macrocrack was generated as load increased, and finally the beam collapsed. Fig. 9(b) depicts the macrocrack and the crushed compression head of the long beam. As it can be observed in Fig. 8, the microcrack formation phase appeared at different load level due to the different amount of reinforcement used for each beam. This circumstance generated the difference in the stiffness in the microcrack stabilization phase and the consequent macrocrack apparition. Moreover, at the end of the test it was observed that even though the reinforcement was yielded for both beams, the UHPFRC compression head was more crushed even generating spalling as concrete was more stressed for the case of JE-1(ϕ20) than for JE-2(ϕ16) due to the different amount of reinforcement used.

In addition, Fig. 10 depicts the equivalent bending stress (σ) – average strain at the mid-span section at the compression displacement transducer's height (ε_{comp}) and at the tension displacement transducer's height (ε_{tens}), as it can be seen in the disposition of the horizontal displacement transducers in Fig. 5(c). The equivalent bending stress was obtained after applying Eq. (2) to the experimental load (P) expressed in N, and the average strains for compression and tension were obtained dividing the respective horizontal displacements by the gauge length (here considered 160 mm).

$$\sigma = 0.0005 \cdot P \quad \left(\mathrm{N/mm^2}\right) \tag{2}$$

As it is shown in Fig. 10, the compression and tension stress-strain response changed the stiffness from the uncracked phase to the microcrack stabilization phase when the microcraking formation developed. Due to the development of the UHPFRC's characteristic distributed microcracking pattern, the block of compressive stresses in the mid-span section changed its elastic stiffness and the tensile stresses in the microcracked part of the section were transferred from the concrete to the reinforcement progressively via tension-stiffening effect. Moreover, it can be observed that the stiffness in the microcrack stabilization phase remained relatively constant until the macrocrack localization generated as a consequence of the coalescence of microcracks from previous phase. Therefore, it can be emphasized this important consequence of the tension-stiffening effect for UHPFRC: the stiffness remains constant during the microcracking stabilization phase from the microcrack formation to the macrocrack localization. This means that the microcraked UHPFRC behaves linearly due to the presence of the fibers that generates an extra of strength in the concrete matrix when the

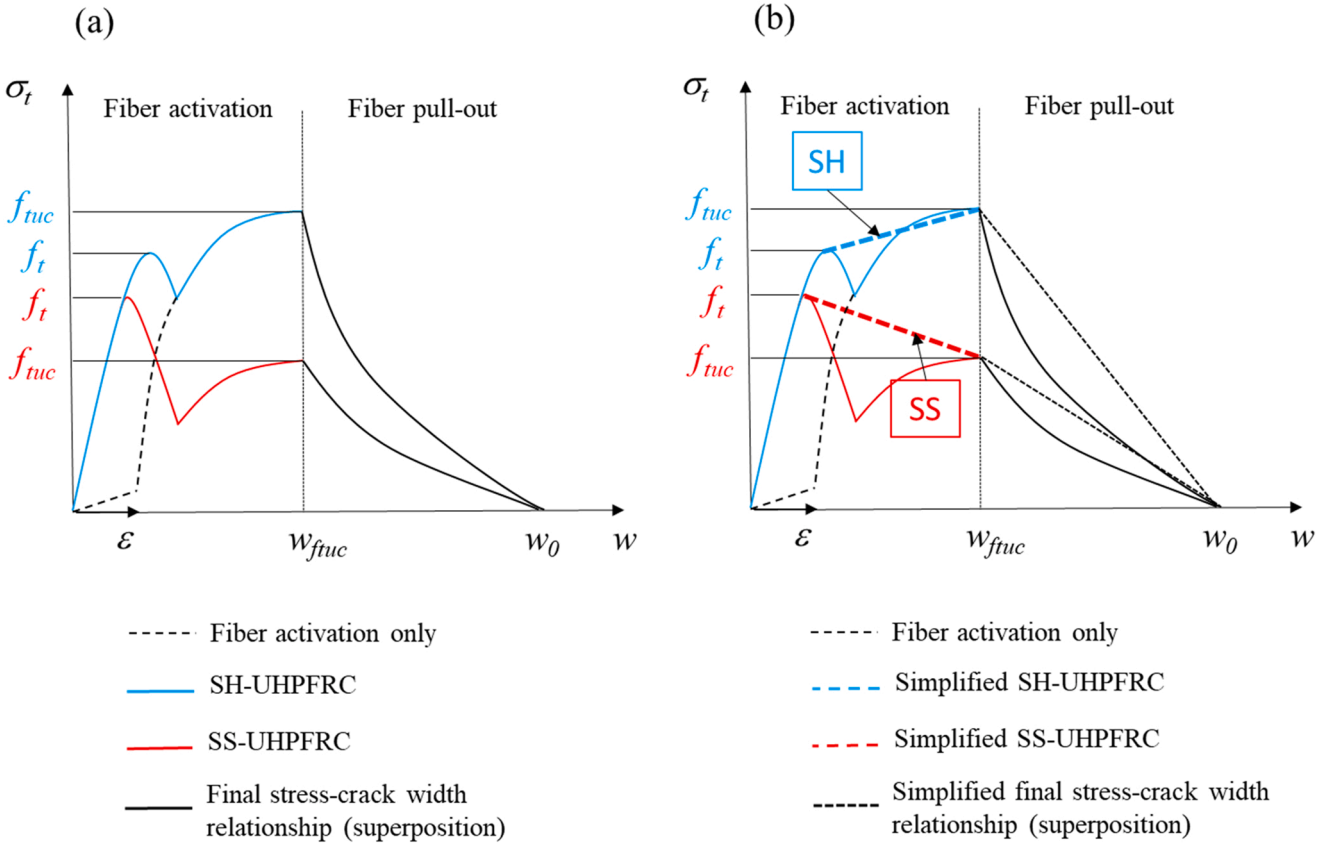

Fig. 13. (a) Mechanical tensile behavior for FRC and UHPFRC in [1,57,58] and (b) simplified tensile constitutive behavior for UHPFRC numerical modeling and design assumed in [46,47,49].

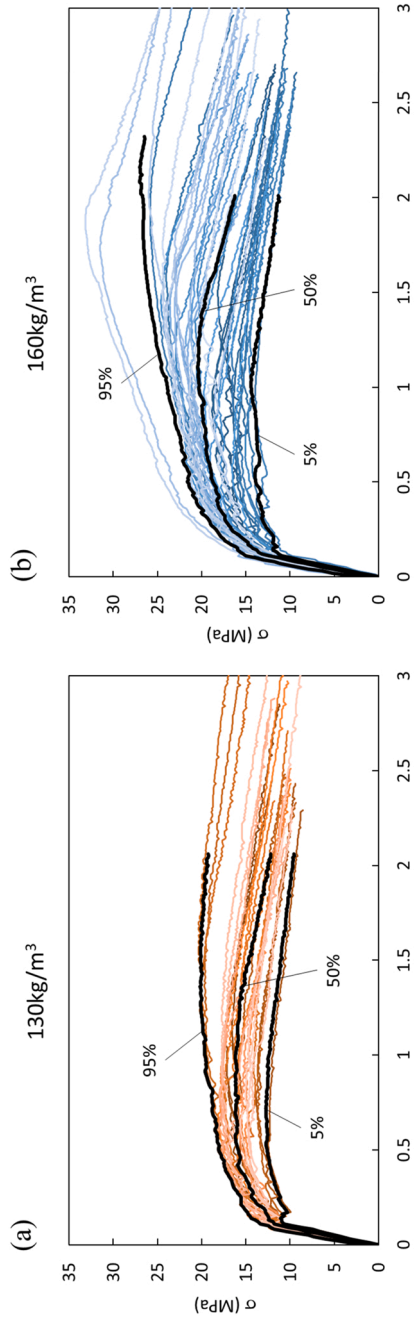

Fig. 14. σ-δ curve from 4PBT of the specimens with (a) 130 kg/m^3 and (b) 160 kg/m^3 of fiber contents.

Table 4
Average and CV of constitutive parameters of UHPFRC XS1 dosage.

XS1: 160 kg/m^3 of steel fibers						
	f_t (MPa)	f_{tu} (MPa)	ε_{tu} (‰)	E (MPa)	w_o (mm)	f_c (MPa)
Average	9.59	8.08	4.85	49,651	2.91	154.27
CV (%)	7.67	20.78	33.83	4.79	17.30	9.92

Table 5
Characteristic constitutive tensile parameters and softening correction.

130 kg/m^3 of steel fibers					
Charact. σ-δ	f_t (MPa)	f_{tuc} (MPa)	ε_{tu} (‰)	E (MPa)	w_o (mm)
5%	6.59	5.27	1.43	44,700	2.81
50%	7.56	7.05	1.18	49,000	2.43
95%	8.88	7.85	4.38	53,600	4.45
160 kg/m^3 of steel fibers					
Charact. σ-δ	f_t (MPa)	f_{tuc} (MPa)	ε_{tu} (‰)	E (MPa)	w_o (mm)
5%	7.01	5.57	4.09	46,300	2.55
50%	8.89	8.14	3.69	48,700	2.42
95%	10.22	10.23	7.56	51,800	3.31

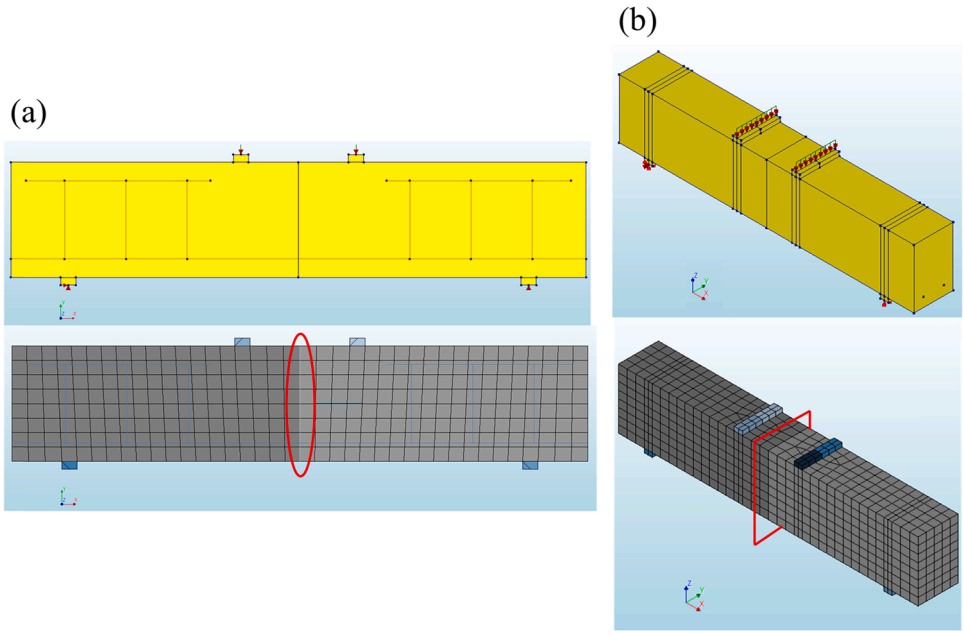

Fig. 15. Geometry and mesh for reinforced short beams: 2D-NLFEM (a) and 3D-NLFEM (b).

microcrack appears allowing the development of more microcracks and not transferring entirely the stress to the reinforcement. This extra strength could be translated in an extra crack energy in the microcracking process that is maintained during the microcraking stabilization phase due to the fiber effect resulting in a relatively constant average behavior and therefore in a relatively constant tension-stiffening effect. Therefore, in this work the tension-stiffening phenomenon was considered implicitly in the bending response taking into account not only the collaboration of the tensile strength from the concrete between cracks, but also considering the residual strength in the proper crack due to the effect of fibers.

2.3. Material characterization

In order to characterize the mechanical behavior of the UHPFRC used in each mix, a set of 100 mm cubic specimens for the compression test and 500×100×100mm unreinforced specimens for the 4PBT was cast together with beams (Fig. 11). Twenty-two

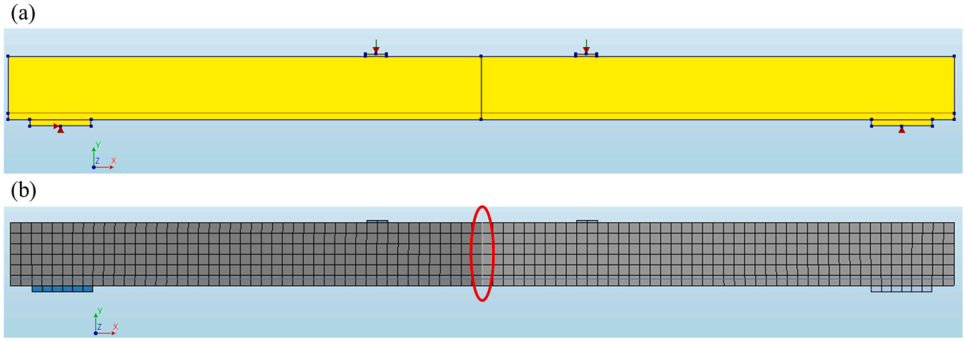

Fig. 16. Geometry (a) and 2D mesh (b) for reinforced long beams.

UHPFRC batches were done in the experimental program: 8 batches for UHPFRC with 130 kg/m^3 (32 cubic specimens and 25 unreinforced 4PBT specimens) and 14 batches for UHPFRC with 160 kg/m^3 (61 cubic specimens and 38 unreinforced 4PBT specimens).

To obtain tensile behavior by using bending tests, it is necessary to apply inverse analyses. For this purpose, the authors chose an inverse analysis method: a simplified Four-Point Inverse Analysis method (4P-IA) that was properly developed by the research group for UHPFRC that exhibits strain-hardening (SH) behavior. It is explained in [49,55]. This method has also been calibrated and adapted by the authors of this paper for UHPFRC that exhibits strain-softening (SS) (softening correction) [47,56]. This results in an optimized UHPFRC material constitutive behavior for modeling and design, characterized by a direct reliable defined procedure [47]. According to 4P-IA, to define the assumed tensile behavior (Fig. 12(b)), it is necessary to select specific key points from the experimental 4PBT equivalent bending stress-displacement on the mid-span curve (Fig. 12(a)). Using these points, the parameters defining the assumed simplified trilinear σ-ε/w tensile law (Fig. 12(b)) can be determined by a back-of-the-envelope calculation and a softening correction (f_{tuc}). It is important to note that the tensile constitutive model proposed for both in SH- and SS-UHPFRC in the direct procedure for tensile characterization [46,47] is considered in a simplified way for modeling and design, as in the French standard [40–42]. In the direct procedure the transition between the UHPFRC tensile strength f_t and the UHPFRC corrected ultimate tensile strength f_{tuc} is considered linear (see Fig. 13(b)), neglecting the possible stress valley that could be generated when combining the phenomenon of the softening of the concrete matrix after cracking and the consequent activation of the steel fibers present in it as described in [1,57,58] and shown in Fig. 13. The simplification assumed in Figs. 12 and 13(b) applied to define the direct procedure to characterize the tensile behavior of SH- and SS-UHPFRC for modeling and design was calibrated and validated in [46,47], where the ultimate tensile strain (ε_{tu}) was defined as the relation between the crack opening at f_{tuc} (w_{ftuc}) and the material crack bandwidth or process zone (b_w).

Fig. 14 depicts the 4PBT σ-δ experimental curves obtained from 25 specimens with 130 kg/m^3 of fiber content and 38 with 160 kg/m^3 of fiber. The curves for the average and the bound values (5% and 95% characteristics) are emphasized in Fig. 14.

The compressive strength obtained from the cubic specimens fell within a range of [99.88, 130.56] MPa for the 130 kg/m^3 fiber content, and [114.23, 172.08] MPa for the 160 kg/m^3 fiber content.

The tensile parameters obtained from the prismatic specimens are included within the following ranges: (a) for the specimens with 130 kg/m^3 of fiber content: f_t in [6.48, 9.31] MPa, f_{tu} in [4.65, 8.06] MPa, ε_{tu} in [1.09, 5.20] ‰, E in [39100,53800] MPa, w_0 in [2.00, 4.45] mm and γ in [0.65, 1.08]; (b) for the specimens with 160 kg/m^3 of fiber content: f_t in [6.88, 11.41] MPa, f_{tu} in [4.97, 13.75] MPa, ε_{tu} in [1.37, 8.75] ‰, E in [44100,55100] MPa, w_0 in [1.75, 4.06] mm and γ in [0.59, 1.25].

Moreover, to evaluate the grade of variability of the constitutive parameters for the material characterization of the UHPFRC, the average and the coefficient of variation (CV) of the tensile parameters from the 4P-IA application and the compressive strength obtained from the prismatic and cubic specimens cast using dosage XS1 are shown in Table 4. Even though the f_{tu} and the ε_{tu} parameters exhibited high values of CV that could be attributable to the 4P-IA methodology, they could be considered acceptable for UHPFRC due to the heterogeneity generated by the fibers.

Table 5 summarizes the tensile constitutive parameters of the characteristic curves, which were obtained after applying 4P-IA and the softening correction.

The B500SD steel used for the reinforcement bars was characterized by a bilinear stress-total strain constitutive behavior with strain hardening considering: tensile strength (f_{st}) of 500 MPa, ultimate tensile strength (f_{stu}) of 550 MPa, elastic strain ($\varepsilon_{st,el}$) of 0.0025, ultimate tensile strain ($\varepsilon_{st,u}$) of 0.05 and elastic modulus (E_s) of 200,000 MPa.

3. Numerical model

Non-linear 2D and 3D finite element models (NLFEM) were developed to model the reinforced UHPFRC specimens using the DIANA FEA Finite Element software [59]. These models start from the NLFEM defined by the authors in [47,48,56,60]. In this case, the main task was to adapt the capabilities of the NLFEM, even with reinforced concrete beams.

To model tensile UHPFRC constitutive behavior, two different approaches were followed: a *Smeared Cracking Approach* and a *Discrete Cracking Approach*. In the *smeared approach*, the constitutive model for UHPFRC was based on a fixed total strain crack model, expressed according to the crack opening curve. For the *discrete approach*, the constitutive model for UHPFRC was based on the discrete

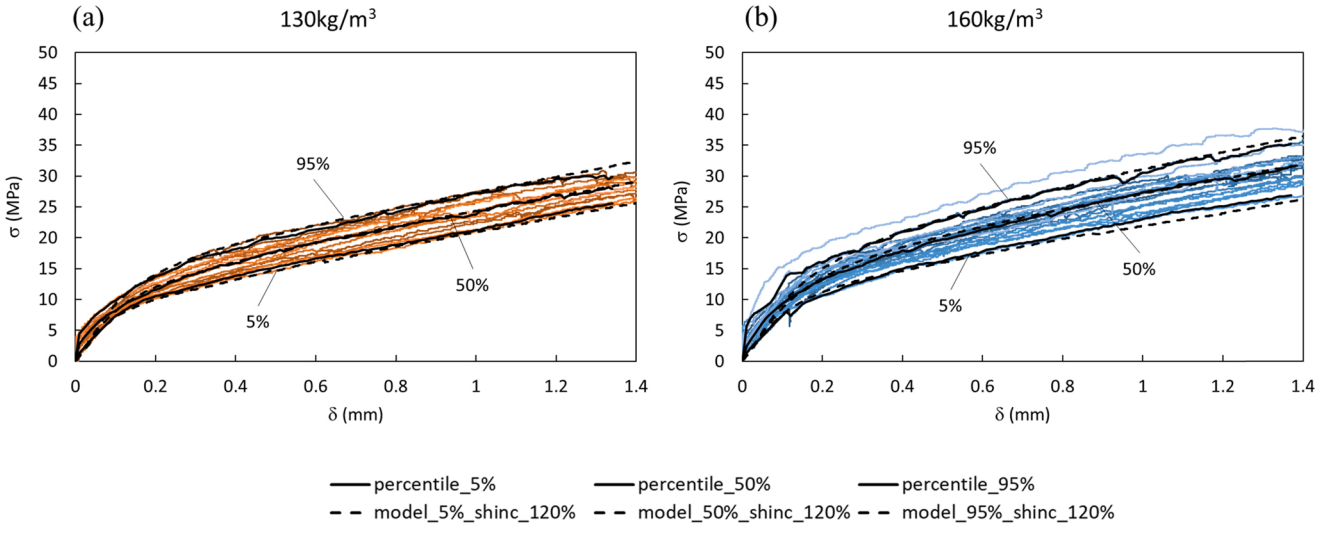

Fig. 17. Experimental vs. numerical σ-δ characteristic response for 5%, 50% and 95% for the short reinforced beams with (a) 130 and (b) 160 kg/m^3 of fiber contents.

Table 6
Shrinkage values for the UHPFRC with short beams.

130 kg/m^3 of steel fibers				
Charact.	Testing day	ε_{cs} (mm/m)	sh_{inc} (%)	$\varepsilon_{csUHPFRC}$ (mm/m)
5%	49	0.34	120	0.75
50%	49	0.34	120	0.75
95%	49	0.35	120	0.77
160 kg/m^3 of steel fibers				
Charact.	Testing day	ε_{cs} (mm/m)	sh_{inc} (%)	$\varepsilon_{csUHPFRC}$ (mm/m)
5%	49	0.34	120	0.75
50%	49	0.35	120	0.77
95%	49	0.38	120	0.84

cracking model as interface behavior. This behavior was implemented only at the central specimen section. The rest of the specimen was modeled by the *Smeared Cracking Approach*.

Reinforcement was modeled using Von Mises strain-hardening elasto-plastic behavior for the steel with a bond-slip behavior between reinforcement and the UHPFRC matrix by the Dorr constitutive model for the interface bond-slip elements.

The results of the UHPFRC characterization obtained by the 4P-IA with softening correction were implemented into the constitutive behavior of the above-described NLFEM. Therefore, the effect of fibers on constitutive tensile behavior was considered with these parameters. Another important effect that was contemplated was concrete shrinkage and its consequences for concrete and reinforcement. In this case, it was taken into account as a material function when the UHPFRC model was defined in the NLFEM using the total strain crack model. Accordingly, the shrinkage function from EN 1992–1–1 Eurocode 2 [43] was employed. From it, the obtained values were incremented as a percentage to be adapted to the UHPFRC response. That is, the total shrinkage strain of UHPFRC ($\varepsilon_{csUHPFRC}$) is defined as Eq. (3), in which the value obtained on the testing day using Eurocode 2 (ε_{cs}) is incremented by different percentages (sh_{inc}) to take into account the influence of shrinkage on UHPFRC. It is important to note that in the numerical model the effect of shrinkage was implemented without considering the possible relaxation of stresses in UHPFRC as a consequence of the effect of creep, i.e. considering the free shrinkage.

$$\varepsilon_{csUHPFRC} = \varepsilon_{cs} \bullet (1 + sh_{inc}/100) \tag{3}$$

Both the short and long reinforced beams were modeled with 2D quadratic plane stress elements (in the 2D model) and 3D quadratic structural isoparametric solid brick elements (in the 3D model) when the *Smeared* and *Discrete Cracking Approaches* were followed. Besides for the *Discrete Cracking Approach*, a quadratic 2D line interface element (in the 2D model) and a quadratic plane 3D interface element (in the 3D model) were placed at the mid-span section to model macrocrack behavior. Fig. 15 shows the mesh used for the *Discrete Cracking Approach* of the NLFEM with short beams: for 2D-NLFEM (Fig. 15(a)) and 3D-NLFEM (Fig. 15(b)). The same concept was applied to long beams (Fig. 16). For the 2D and 3D-NLFEM of the short beams, an element size of 20 mm was used. For the 2D-NLFEM of the long beams, an element size of 50 mm was considered. As the *Discrete Cracking Approach* is not mesh size dependent, it was possible to optimize the time and calculation resources with the mesh size. Reinforcement was modeled discretely using truss bond-slip elements. Load was applied to the steel load plates by gradually increasing displacement. A non-linear analysis was carried out by an incremental-iterative solution procedure.

4. Numerical simulation and discussion

Here the reliability of using the constitutive parameters obtained from the characterization test to evaluate the mechanical response of the UHPFRC-reinforced elements through the NLFEM is analyzed.

4.1. Short beams

In short beams, the characteristic tensile parameters in Table 5, obtained by applying 4P-IA and its softening correction to the characteristic 4PBT σ-δ curves of the 500×100×100 specimens, were implemented into the NLFEM. The numerical response of the obtained short reinforced beams was compared to the experimental response depicted in Fig. 3.

Fig. 17 shows the characteristic experimental 4PBT σ-δ curves for 5%, 50% and 95% of the short reinforced beams tested for the experimental program (continuous black lines) compared to the characteristic response of the NLFEM when the *discrete approach* is used (discontinuous ones). As observed, the model curves accurately fit the experimental ones for each level. This demonstrates not only the reliability of the developed NLFEM, but also the coherence of the process. That is, if the characteristic tensile constitutive parameters used to mechanically characterize UHPFRC were implemented into the NLFEM of the reinforced beams, the numerical response would accurately fit the experimental one at the 5%, 50% and 95% percentile levels.

It is important to pay attention to the shrinkage value used to calibrate the model. To fit the results with this accuracy, a 120% increment in the shrinkage value calculated from EN 1992–1–1 Eurocode 2 [43] was needed in the NLFEM. In Table 6, the shrinkage values (ε_{cs}) for each characteristic level and the 120% increment (sh_{inc}) required to accurately fit the results are provided. The total

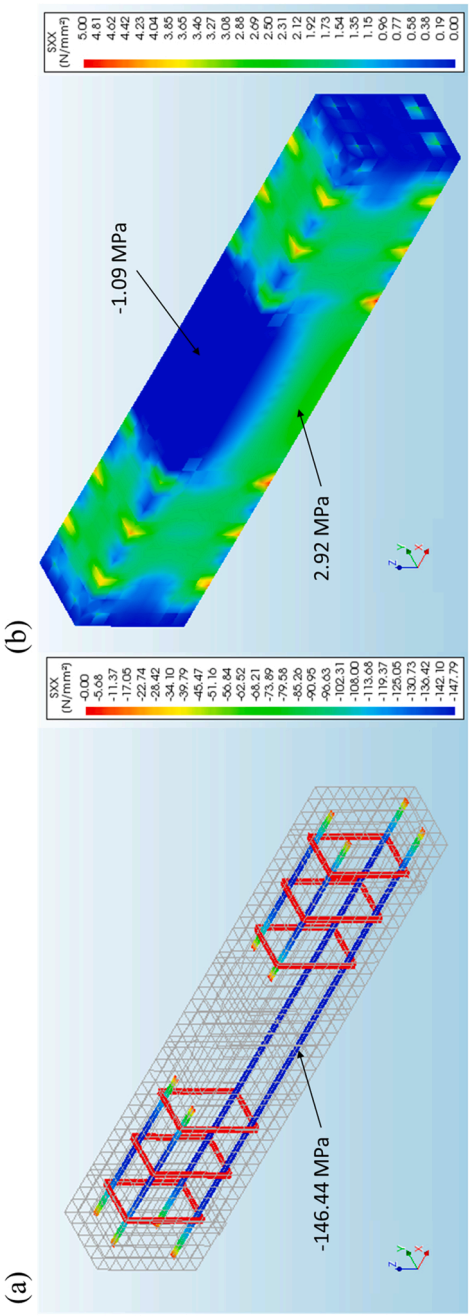

Fig. 18. Shrinkage stresses in the 3D NLFEM (a) reinforcement and (b) UHPFRC.

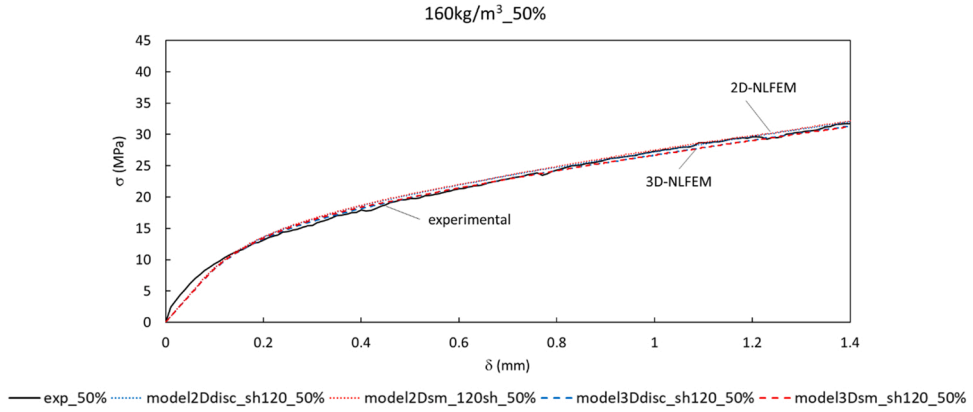

Fig. 19. Comparison between the NLFEM approaches for 160 kg/m^3 fiber content.

Table 7
Mechanical UHPFRC properties for long beams.

160 kg/m^3 of steel fibers						
Beam	f_t (MPa)	f_{tuc} (MPa)	ε_{tu} (‰)	E (MPa)	w_o (mm)	f_c (MPa)
JE-1(ϕ20 mm)	9.43	10.44	6.25	54,500	3.13	165.77
JE-2(ϕ16 mm)	8.95	8.48	3.74	50,000	3.14	172.08

shrinkage strain of UHPFRC ($\varepsilon_{csUHPFRC}$) was calculated using Eq. (3), and fell within the range of [0.75, 0.84] mm/m. Fig. 18 depicts the stress consequences that the shrinkage effect on the UHPFRC beam with 160 kg/m^3 of steel fiber content generates by taking into account the 50% characteristic tensile parameters in 3D NLFEM in both reinforcement (Fig. 18(a)) and the UHPFRC body (Fig. 18(b)). In Fig. 18(b), only the tensile stress range is illustrated to emphasize the stresses due to the shrinkage effect on UHPFRC. This effect followed the reinforcement path.

Fig. 19 compares both NLFEM approaches (*smeared* and *discrete*) to the experimental σ-δ response for the characteristic 50% level. The tensile constitutive parameters for 50% in Table 5 were implemented in both NLFEM approaches and compared. As observed, the numerical model fits the experimental response very well. The elastic and multicrack stages are accurately represented. Unlike the behavior achieved with the unreinforced specimens in the 4PBT in [48], it can be noted that the differences between both the NLFEM hypotheses were not significant, allowing the use of either of the two depending on the convenience when reinforced specimens are modeled. This means that the presence of reinforcement notoriously influenced specimens' mechanical behavior when the macrocrack appeared. At that time, UHPFRC lost its bearing capacity and stress was progressively transmitted to reinforcement through the "tension-stiffening" mechanism. This effect gave a close response between the *smeared* and *discrete* NLFEM *approaches*. We can also observe how the differences between the 2D and 3D NLFEM are negligible. The model's accuracy was good and both the models with the *smeared* and *discrete approaches* proved completely reliable. This fact justified that, for long beams, only the 2D model was used to avoid the amount of calculation time and sources spent for the 3D one. The 3D model was employed only to observe such important 3D effects like shrinkage (Fig. 18).

4.2. Long beams

Table 7 contains the average tensile parameters for the 500×100×100mm unreinforced specimens cast together with the beams for the UHPFRC mechanical characterization. Specimens were tested in a 4PBT and the σ-δ average curves were obtained for the specimens cast with JE-1 (ϕ20 mm) and JE-2 (ϕ16 mm), respectively. These σ-δ curves were located near the 95% percentile curve in Fig. 14(b). Therefore, a good tensile response of these UHPFRC batches can be expected. Then the 4 P-IA analysis and softening correction were applied to obtain the average tensile constitutive behavior for each beam. In Table 7, the average compressive strength from the 100-mm cubic specimens is also reported. The obtained UHPFRC mechanical parameters were implemented into the *discrete approach* of 2D-NLFEM. Several results were analyzed after running the model for long beams.

Fig. 20 shows the equivalent bending stress (σ)-displacement at the mid-span(δ) curves for the experimental test obtained after applying Eq. (2) to the experimental load expressed in N (P)-displacement at the mid-span curves (Fig. 8), and compared to the response of the applied model by considering three cases based on how shrinkage was taken into account from Eq. (3): with no shrinkage ("model no sh"), with shrinkage calculated as in EN 1992–1–1 Eurocode 2 [43] considering $sh_{inc} = 0$ in Eq. (3) ("model 0% sh-inc"), and with a 90% incremented shrinkage value considering $sh_{inc} = 90$ in Eq. (3) ("model 90%sh-inc") in beam JE-1% and 120% considering $sh_{inc} = 120$ in Eq. (3) ("model 120%sh-inc") in beam JE-2. As seen in Fig. 20 the shrinkage variation in the NLFEM defined by means of Eq. (3) affected directly the microcrack formation phase (see Fig. 8) which in turn affected the initiation of the

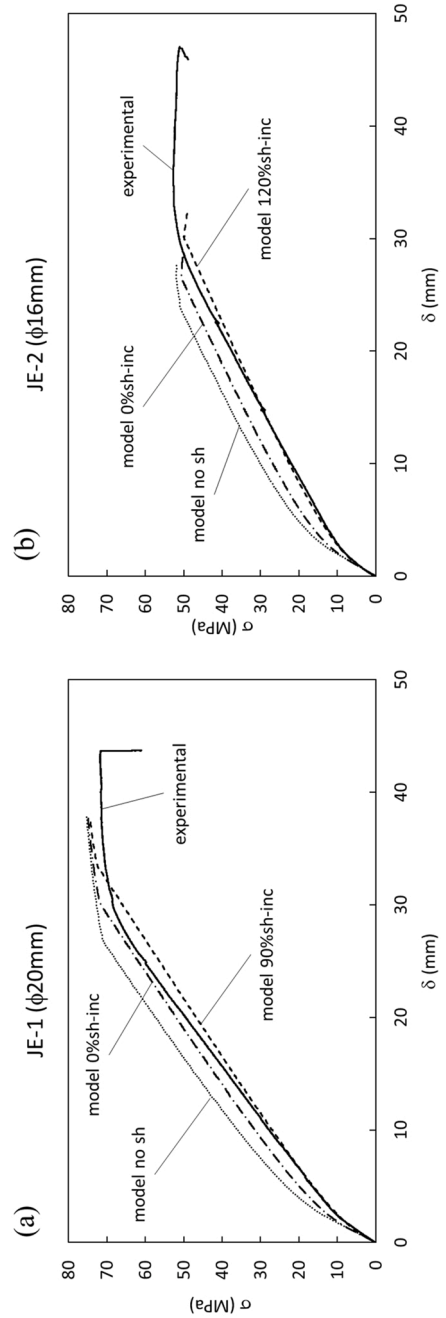

Fig. 20. σ-δ curves for the (a) JE-1 and (b) JE-2 beams.

Table 8
Shrinkage values at 49 days for long beams.

160 kg/m^3 of steel fibers				
Beam	Testing day	ε_{cs} (mm/m)	sh_{inc} (%)	$\varepsilon_{csUHPFRC}$ (mm/m)
JE-1 (ϕ20 mm)	49	0.37	90	0.70
JE-2 (ϕ16 mm)	49	0.37	120	0.81

tension-stiffening effect that allows the microcrack stabilization phase in the bending response of the beams. Therefore, the shrinkage value was calibrated in the NLFEM according to the experimental microcrack formation phase trying to fit the experimental microcrack stabilization phase. As observed in Fig. 20, the model very well fits the experimental curve when a 90% shrinkage increment was applied at 49 days for JE-1 and one of 120% for JE-2. Table 8 presents these values for the two tested beams. The total shrinkage strain of UHPFRC ($\varepsilon_{csUHPFRC}$), calculated by Eq. (3) for these two beams, fell within the range of [0.70, 0.81] mm/m.

As a result, the values of the concrete shrinkage strains obtained for both short (Table 6) and long beams (Table 8) fell within the range of [0.70, 0.84] mm/m. This is consistent with the range of [0.60, 0.90] mm/m for UHPFRC with a non heat treatment and a water/cement ratio of ≤ 0.25, which other researchers considered in [1,3–5].

For more details, Fig. 21 offers the stress profile at the mid-span section of the two beams due to UHPFRC shrinkage ($\varepsilon_{csUHPFRC}$) 49 days after they were cast before starting the experimental test. As we can see, the generated stress is very important given the influence of the reinforcement bars embedded in the UHPFRC matrix. So it can be deduced that the UHPFRC in the vicinity of reinforcement was highly stressed in tension, and even came close to the f_t value before the test started. This means that the concrete there was pre-stressed near cracking and, consequently, its bearing capacity reduced. The effect on reinforcement was the opposite. Longitudinal bars were compressed and, as a result, they displayed pre-compression before the test, which led to a higher bearing capacity for the bending test. When comparing both graphs, it is worth noting that the JE-1 beam achieved more stress in both compression (h = 300 mm) and tension (h = 0 mm) than the JE-2 beam. Furthermore, reinforcement was less compressed in JE-1 than in JE-2. These results are absolutely logical if the different amounts of reinforcement between JE-1 (2ϕ20 mm) and JE-2 (2ϕ16 mm) are considered. So after analyzing these results, it can be concluded that the shrinkage effect was very strong on UHPFRC and, consequently, its influence on the beam's structural response was not at all negligible.

Regarding the cracking process under load and the corresponding reinforcement stresses, Figs. 22 and 23 illustrate the crack opening and reinforcement stress in the central part of the JE-1 and JE-2 beam in two stages: microcracking stage (σ = 30 MPa for JE-1 and σ = 20 MPa for JE-2) and upon collapse. As observed, Figs. 22 and 23 show that when using NLFEM, the cracking process of the UHPFRC beams develops as in the experimental test. This figure very well illustrates the appearance of microcracking and how this affects reinforcement stresses, while concrete loses its tensile capacity. Upon collapse, the cracking process concentrated on one macrocrack and, consequently, the tensile stress of reinforcement increased at this point until its plasticity level was reached. As seen in both figures, the cracking pattern differed depending on the corrected hardening ratio (γ_c), defined as the quotient between the corrected ultimate tensile strength (f_{tuc}) and tensile strength (f_t) of the developed UHPFRC constitutive behavior. As JE-1 exhibited strain-hardening ($\gamma_c > 1$) (see Table 7), the cracking pattern was smeared with mapped cracking in the microcracking stage and progressed to a more concentrated area with a wider crack width as the macrocrack appeared. For JE-2, the cracking pattern was also smeared in the microcracking stage, but was slightly different from JE-1. As the UHPFRC of JE-2 exhibited strain softening ($\gamma_c < 1$) (see Table 7), the microcracking stage had cracks concentrated in clear zones and the macrocrack developed from one of these zones. Therefore, the cracking process simulated by the NLFEM was most reliable and represented reality very well at both the service and ultimate load levels.

5. Design considerations for UHPFRC

Some design aspects of the bending section under serviceability and ultimate conditions were considered. This was done to know if the traditional design under bending and normal forces would be accurate enough for the reinforced UHPFRC cross-sections, and it also aimed to evaluate how fibers actually contributed to flexure strength.

5.1. Serviceability level

In cracking behavior terms, it is worth mentioning that no clear formation of macrocracks up to the failure conditions was observed on either short beams or long ones. Under service conditions, the following three stages were noted instead for both beam types: (1) uncracked; (2) microcrack formation; (3) stabilized microcracking (see Figs. 17 and 20).

In load-deflection response terms, flexural stiffness remained relatively constant in the stabilized microcracking stage. The experimental flexural stiffness (EI_{exp}) was determined in all the tested beams. The obtained values are shown in Table 9. Moreover, the flexural stiffness (EI_{cr}) calculated when considering the contribution of only the uncracked concrete part and longitudinal reinforcement was also obtained. This simplified way of calculating flexural stiffness followed the traditional approach, which considers the cracked section, just as several codes suggest for estimating RC member deflections; e.g. as in EN 1992–1–1:2004 [43].

It can be outlined that the flexural stiffness of long beams under serviceability conditions came very close to the fully cracked cross-section stiffness. However in short beams, the value of the calculated stiffness was higher than that of the experimental one. In any

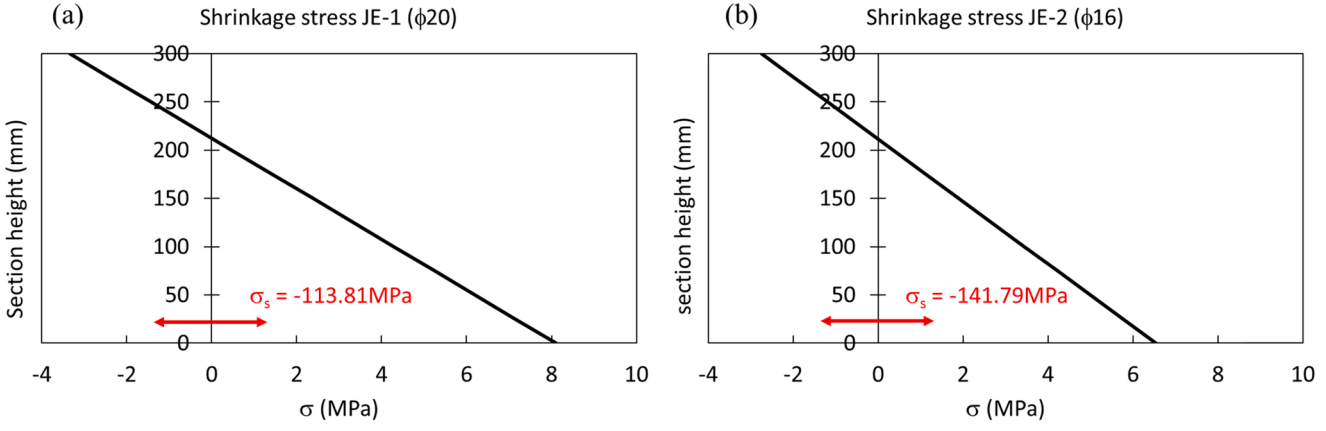

Fig. 21. Shrinkage stresses at the mid-span section for the (a) JE-1 and (b) JE-2 beams at 49 days.

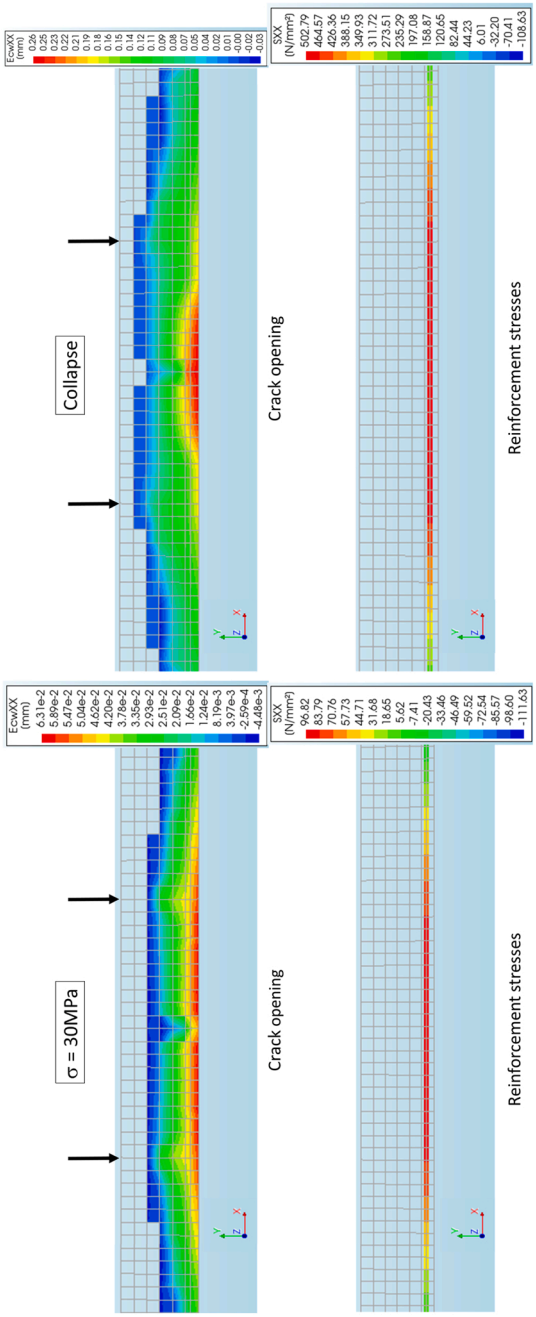

Fig. 22. Crack opening and reinforcement stresses at 30 MPa of load and upon collapse for the JE-1 beam.

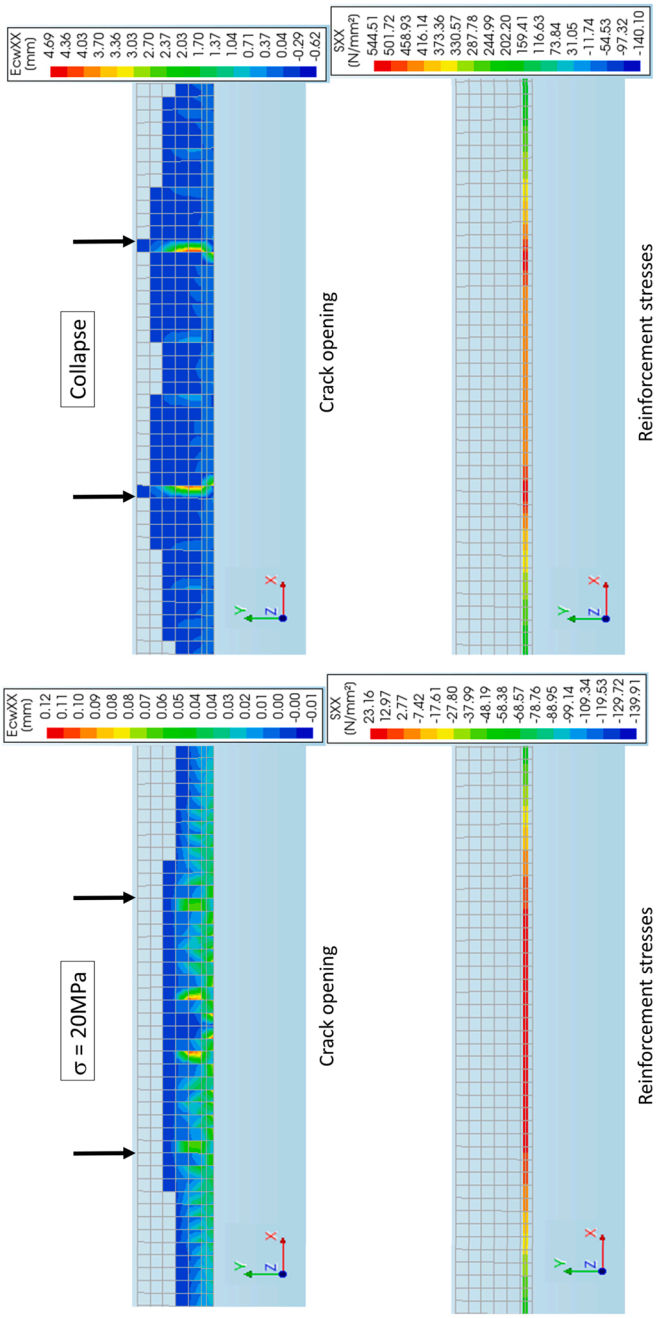

Fig. 23. Crack opening and reinforcement stresses at 20 MPa of load and upon collapse for the JE-2 beam.

Table 9
Cross-section flexural stiffness under serviceability conditions.

Beam	EI_{exp} [kN·m^2]	EI_{cr} [kN·m^2]	EI_{exp} / EI_{cr}
Short 130 kg/m^3	182.8	228.9	0.799
Short 160 kg/m^3	208.3	228.7	0.911
JE-1 (ϕ20 mm)	5349.6	5395.4	0.992
JE-2 (ϕ16 mm)	3843.0	3817.5	1.007

case, the poorest reinforced beam (the short beam with 130 kg/m^3) reached nearly 80% of total flexural stiffness.

According to Bischoff [61], tension-stiffening factor β can be obtained for defining the element's member response. Setting β to equal 1 gives a bilinear response with constant tension-stiffening that represents an upper bound on member stiffness, as shown in Fig. 24 for long beams. A β value of 0 gives a lower bound with no tension-stiffening, which essentially provides the I_{cr} response. Both long beams showed a nearly full-tension stiffening response as an experimental β value close to 1 was obtained under serviceability conditions (Fig. 24). Therefore, the control of deflections in those beams exhibiting full-tension stiffening can be carried out in the whole service stage (stabilized microcracking) by assuming an effective moment of inertia I_e given by Bischoff's proposed expression [61] and considering (β = 1):

$$I_e = \frac{I_{cr}}{1-\eta \cdot \beta_\bullet}(M_{cr}/M_a) \le I_g \quad \text{where} \quad \eta = 1 - I_{cr}/I_g \tag{4}$$

5.2. Ultimate level

The constitutive equation to be used in the axial and bending analysis in the ultimate limit state requires converting the stress-crack opening branch of the tensile properties obtained in Table 7 into a continuous stress-strain diagram. To do so, a characteristic length that equaled 2 h/3 = 200 mm was assumed according to NF P18–470 [40], along with a coefficient of orientation K = 1.25, to model the tensile properties of UHPFRC [40]. Finally, the concrete compressive strength was assumed as that obtained in a cylinder ($f_{c,cyl}$), which can be related to cubic strength with a difference of −15 MPa [40]. By way of example, Fig. 25(a) presents the constitutive equation assumed in the design analysis under bending for the JE-2 beam. The cross-section's possible plain strain distributions in the ultimate limit states are limited by either a peak strain in the most compressed fiber that equals $f_{c,cyl}$ / E or a maximum tensile strain in the longitudinal reinforcement of 10‰. So by applying the axial equilibrium equation, the location of the neutral axis (x_0) is obtained, and the moment equilibrium equation allows maximum bending moment ($M_{u,cal}$) that the reinforced UHPFRC cross-section can resist to be evaluated (Fig. 25(b)). In the presented calculations, no safety coefficients were taken into account to be compared to the maximum bending moment achieved in the test ($M_{u,exp}$).

The calculations for both long beams (JE-1 and JE-2), and the comparison made to the obtained experimental results, are summarized in Table 10. It is worth mentioning that predictions are relatively accurate, but very much depend on not only the axial tensile force that fibers in tension can carry, but also on the tensile force on longitudinal bars, which reach their yielding stress on both beams. Fibers carry a tension of 34.1% in JE-1 and one of 38.7% in JE-2 of the total tensile force required in the section equilibrium. Therefore, fibers play a significant role in the beam's flexural strength despite them not collaborating directly with the resisted bending moment. For instance, only 2.0 kN·m was resisted by the fibers in the JE-2 beam (Fig. 25(c)). It should be noted that predictions were based on the tensile properties affected by a K coefficient of 1.25, which would result in a lower flexure strength estimation. In the studied cases, K= 1.25 can be considered a reasonable orientation factor given the obtained $M_{u,exp}/M_{u,cal}$ ratios.

6. Concluding remarks

This paper presents a study on flexural reinforced UHPFRC tensile behavior that deals with important aspects, such as the shrinkage and the particular crack pattern of this concrete. An experimental program of reinforced UHPFRC beams was carried out on two different scales. Furthermore, a non-linear finite element model (NLFEM) was developed to validate the employed UHPFRC characterization method and its numerical implementation at material level. Finally, some design aspects of reinforced UHPFRC cross-sections with bending and axial forces under serviceability and failure conditions are addressed and compared to the beams included in the experimental program. The following conclusions can be drawn:

In the experimental bending response of the reinforced UHPFRC beams, two different stages were distinguished: a first stage with greater stiffness, where uncracked concrete and reinforcement work together; a second stage with lesser stiffness, where a microcracking process takes place and the tension-stiffening phenomenon develops. In the second stage, microcracks grow in a smeared way by covering part of the span between supports (the so-called process zone) as load increases. When this stage ends, the concentration in one macrocrack takes place as a consequence of the coalescence of microcracks from previous stage leading to the collapse.

During the experimental test of the reinforced UHPFRC beams, the stiffness in the second stage of the bending response remained relatively constant until the macrocrack localization. Therefore, in this work the tension-stiffening phenomenon was considered implicitly in the bending response taking into account not only the collaboration of the tensile strength from the concrete between cracks, but also considering the residual strength in the proper crack due to the effect of fibers.

When the characteristic tensile constitutive parameters used to mechanically characterize UHPFRC are implemented into the

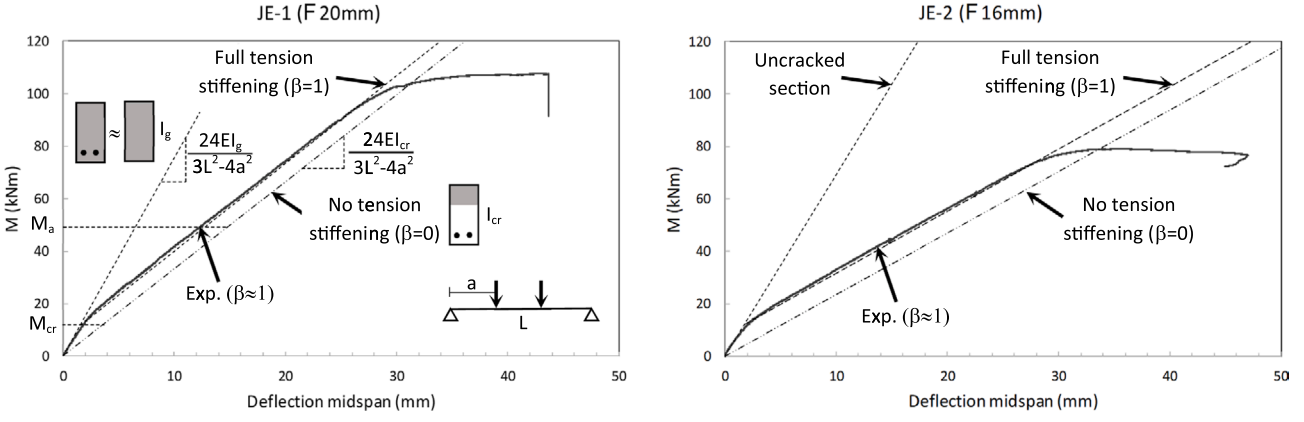

Fig. 24. Deflection comparison of long beams with tension-stiffening factors β.

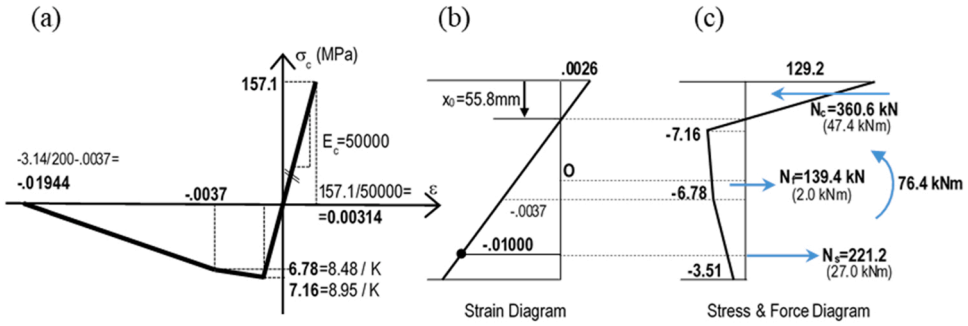

Fig. 25. Flexure strength estimation of the JE-2 beam: (a) assumed constitutive law, (b) strain diagram; (c) stress and force diagram.

Table 10
Comparison between the predicted and experimental values upon failure.

Beam	$M_{u,exp}$ [kN·m]	$M_{u,cal}$ [kN·m]	$M_{u,exp}$ / $M_{u,cal}$	x_0 [mm]	N_c [kN]	N_f [kN]	N_s [kN]
JE-1 (ϕ20 mm)	107.4	114.2	0.94	69.6	524.5	178.9	345.6
JE-2 (ϕ16 mm)	79.1	76.4	1.04	55.8	360.6	139.4	221.2

NLFEM of reinforced beams, the numerical response accurately fitted the experimental one at the 5%, 50% and 95% percentile levels. This result demonstrates the reliability of the developed NLFEM, as well as the coherence of the UHPFRC tensile material characterization process.

The model was developed using two different approaches: *smeared* and *discrete*. The differences in the results obtained with the two approaches were negligible, unlike the response acquired with the unreinforced specimens in 4PBT. It is stated that reinforcement notoriously influences the mechanical behavior of specimens when macrocracking appears via the "tension-stiffening" mechanism.

From the NLFEM application, it was deduced that the UHPFRC's shrinkage affects the second stage of the bending response of the reinforced UHPFRC beams where the microcrack formation and microcrack stabilization phases take place.

Given its particular dosage, UHPFRC is a concrete type that undergoes a high shrinkage level. By using the NLFEM, the shrinkage strain was deduced within a range of [0.70, 0.84] mm/m, which is consistent with other research works. This can generate internal stresses before test starts, which need to be taken into account given the potential influence on the beam's service response. According to the NLFEM simulation, the internal tensile stresses in the UHPFRC matrix came close to the tensile strength (f_t). Therefore, the developed NLFEM is able to predict the structural response of UHPFRC by considering the shrinkage effect.

NLFEM is able to simulate and identify the different cracking pattern based on the UHPFRC constitutive behavior; that is, depending on the corrected hardening ratio. Consequently, the cracking process simulated by the NLFEM is completely reliable and very well represents reality at both the service and ultimate load levels.

The flexure strength predictions of long beams are quite accurate and very much depend on the tensile force that fibers can carry out. Both beams showed a nearly full-tension stiffening response ($\beta \approx 1$) under serviceability conditions, which simplifies the evaluation of the effective moment of inertia to control deflections.

Declaration of Competing Interest

The authors declare that they have no known competing financial interests or personal relationships that could have appeared to influence the work reported in this paper.

Acknowledgments

This work forms part of Project "BIA2016–78460-C3–1-R" supported by the State Research Agency of Spain and the project "Rethinking coastal defence and Green-energy Service infrastructures through enHancEd-durAbiLity high-performance cement-based materials-ReSHEALience", funded by the European Union Horizon 2020 research and innovation programme under GA No 760824.

References

[1] E. Fehling, M. Schmidt, J. Walraven, T. Leutbecher, S. Fröhlich, Ultra-High Performance Concrete UHPC: Fundamentals, Design, Examples, John Wiley & Sons, 2014.
[2] D.-Y. Yoo, N. Banthia, Mechanical properties of ultra-high-performance fiber-reinforced concrete: a review, Cem. Concr. Compos. 73 (2016) 267–280.
[3] T. Xie, C. Fang, M.S. Mohamad Ali, P. Visintin, Characterizations of autogenous and drying shrinkage of ultra-high performance concrete (UHPC): an experimental study, Cem. Concr. Compos. 91 (2018) 156–173, https://doi.org/10.1016/j.cemconcomp.2018.05.009.
[4] C. Fang, M. Ali, T. Xie, P. Visintin, A.H. Sheikh, The influence of steel fibre properties on the shrinkage of ultra-high performance fibre reinforced concrete, Constr. Build. Mater. 242 (2020), 117993, https://doi.org/10.1016/j.conbuildmat.2019.117993.

[5] D.-Y. Yoo, N. Banthia, Y.-S. Yoon, Effectiveness of shrinkage-reducing admixture in reducing autogenous shrinkage stress of ultra-high-performance fiber-reinforced concrete, Cem. Concr. Compos 64 (2015) 27–36, https://doi.org/10.1016/j.cemconcomp.2015.09.005.
[6] C.-C. Hung, H. Li, H.-C. Chen, High-strength steel reinforced squat UHPFRC shear walls: cyclic behavior and design implications, Eng. Struct. 141 (2017) 59–74, https://doi.org/10.1016/j.engstruct.2017.02.068.
[7] M.A. Sakr, S.R. El-khoriby, T.M. Khalifa, M.T. Nagib, Modeling of RC shear walls strengthened with ultra-high performance fiber reinforced concrete (UHPFRC) jackets, Eng. Struct. 200 (2019), 109696, https://doi.org/10.1016/j.engstruct.2019.109696.
[8] J. Li, C. Wu, H. Hao, An experimental and numerical study of reinforced ultra-high performance concrete slabs under blast loads, Mater. Des. 82 (2015) 64–76, https://doi.org/10.1016/j.matdes.2015.05.045.
[9] J. Li, C. Wu, H. Hao, Z. Wang, Y. Su, Experimental investigation of ultra-high performance concrete slabs under contact explosions, Int. J. Impact Eng. 93 (2016) 62–75.
[10] T. Xie, M.S. Mohamed Ali, P. Visintin, Behaviour and analysis of ultra high performance fibre reinforced concrete (UHPFRC) skew slabs, Eng. Struct. 199 (2019), 109588, https://doi.org/10.1016/j.engstruct.2019.109588.
[11] M. Bastien-Masse, E. Brühwiler, Composite model for predicting the punching resistance of R-UHPFRC–RC composite slabs, Eng. Struct. 117 (2016) 603–616, https://doi.org/10.1016/j.engstruct.2016.03.017.
[12] X. Wu, S. Yu, S. Xue, T.H.-K. Kang, H.-J. Hwang, Punching shear strength of UHPFRC-RC composite flat plates, Eng. Struct. 184 (2019) 278–286, https://doi.org/10.1016/j.engstruct.2019.01.099.
[13] S. Ali Dadvar, D. Mostofinejad, H. Bahmani, Strengthening of RC columns by ultra-high performance fiber reinforced concrete (UHPFRC) jacketing, Constr. Build. Mater 235 (2020), 117485, https://doi.org/10.1016/j.conbuildmat.2019.117485.
[14] H. Aoude, F.P. Dagenais, R.P. Burrell, M. Saatcioglu, Behavior of ultra-high performance fiber reinforced concrete columns under blast loading, Int. J. Impact Eng. 80 (2015) 185–202.
[15] S. Astarlioglu, T. Krauthammer, Response of normal-strength and ultra-high-performance fiber-reinforced concrete columns to idealized blast loads, Eng. Struct. 61 (2014) 1–12.
[16] H. Ji, C. Liu, Ultimate shear resistance of ultra-high performance fiber reinforced concrete-normal strength concrete beam, Eng. Struct. 203 (2020), 109825, https://doi.org/10.1016/j.engstruct.2019.109825.
[17] V. Kodur, R. Solhmirzaei, A. Agrawal, E.M. Aziz, P. Soroushian, Analysis of flexural and shear resistance of ultra high performance fiber reinforced concrete beams without stirrups, Eng. Struct. 174 (2018) 873–884, https://doi.org/10.1016/j.engstruct.2018.08.010.
[18] F. Baby, P. Marchand, M. Atrach, F. Toutlemonde, Analysis of flexure-shear behavior of UHPFRC beams based on stress field approach, Eng. Struct. 56 (2013) 194–206, https://doi.org/10.1016/j.engstruct.2013.04.024.
[19] P. Rossi, D. Daviau-Desnoyers, J.-L. Tailhan, Probabilistic numerical model of cracking in ultra-high performance fibre reinforced concrete (UHPFRC) beams subjected to shear loading, Cem. Concr. Compos. 90 (2018) 119–125.
[20] D.-Y. Yoo, N. Banthia, Y.-S. Yoon, Experimental and numerical study on flexural behavior of ultra-high-performance fiber-reinforced concrete beams with low reinforcement ratios, Can. J. Civ. Eng. 44 (2017) 18–28.
[21] R. Solhmirzaei, V.K.R. Kodur, Modeling the response of ultra high performance fiber reinforced concrete beams, Procedia Eng. 210 (2017) 211–219.
[22] D.-Y. Yoo, Y.-S. Yoon, Structural performance of ultra-high-performance concrete beams with different steel fibers, Eng. Struct. 102 (2015) 409–423.
[23] I.-H. Yang, C. Joh, B.-S. Kim, Flexural response predictions for ultra-high-performance fibre-reinforced concrete beams, Mag. Concr. Res. 64 (2012) 113–127.
[24] I.H. Yang, C. Joh, B.-S. Kim, Structural behavior of ultra high performance concrete beams subjected to bending, Eng. Struct. 32 (2010) 3478–3487, https://doi.org/10.1016/j.engstruct.2010.07.017.
[25] D.-Y. Yoo, N. Banthia, Y.-S. Yoon, Predicting the flexural behavior of ultra-high-performance fiber-reinforced concrete, Cem. Concr. Compos. 74 (2016) 71–87, https://doi.org/10.1016/j.cemconcomp.2016.09.005.
[26] J.R. Deluce, Cracking behaviour of steel fibre reinforced concrete containing conventional steel reinforcement, Dr. Diss. (2011).
[27] G. Kaklauskas, V. Tamulenas, M.F. Bado, D. Bacinskas, Shrinkage-free tension stiffening law for various concrete grades, Constr. Build. Mater. 189 (2018) 736–744.
[28] M. Albitar, M.S.M. Ali, P. Visintin, Evaluation of tension-stiffening, crack spacing and crack width of geopolymer concretes, Constr. Build. Mater. 160 (2018) 408–414.
[29] A.B. Sturm, P. Visintin, D.J. Oehlers, R. Seracino, Time-dependent tension-stiffening mechanics of fiber-reinforced and ultra-high-performance fiber-reinforced concrete, J. Struct. Eng. 144 (2018), 4018122.
[30] C.-C. Hung, H.-S. Lee, S.N. Chan, Tension-stiffening effect in steel-reinforced UHPC composites: constitutive model and effects of steel fibers, loading patterns, and rebar sizes, Compos. Part B Eng. 158 (2019) 269–278.
[31] G.H. Mahmud, Z. Yang, A.M.T. Hassan, Experimental and numerical studies of size effects of Ultra High Performance Steel Fibre Reinforced Concrete (UHPFRC) beams, Constr. Build. Mater. 48 (2013) 1027–1034, https://doi.org/10.1016/j.conbuildmat.2013.07.061.
[32] M. Singh, A.H. Sheikh, M.S. Mohamed Ali, P. Visintin, M.C. Griffith, Experimental and numerical study of the flexural behaviour of ultra-high performance fibre reinforced concrete beams, Constr. Build. Mater. 138 (2017) 12–25, https://doi.org/10.1016/J.CONBUILDMAT.2017.02.002.
[33] H. Yin, K. Shirai, W. Teo, Finite element modelling to predict the flexural behaviour of ultra-high performance concrete members, Eng. Struct. 183 (2019) 741–755, https://doi.org/10.1016/j.engstruct.2019.01.046.
[34] N. Gowripalan, R.I. Gilbert, Design guidelines for ductal prestressed concrete beams, Ref. Artical, Univ. NSW (2000).
[35] AS 3600-1994, Concrete structures, CommitteeBD/2, Concr. Stand. Aust (1994).
[36] Japan Society of Civil Engineers, Recomendations for design and construction of high performance fiber reinforced composites with multiple fine cracks (HPFRCC), Concr. Eng. Ser. 82 (2008).
[37] J.S. of C.E. (JSCE), Standard specifications for concrete structures, Struct. Perform. Verif. (2007).
[38] H.G. Russell, B.A. Graybeal, H.G. Russell, Ultra-high performance concrete: a state-of-the-art report for the bridge community., United States. Fed. Highw. Adm. No. FHWA-H, 2013: 163.
[39] AASHTO LRFD Bridge Design Specifications, Am. Assoc. State Highw. Transp. Off., 2012.
[40] Association Francaise de Normalisation, Concrete-Ultra-high performance fibre-reinforced concrete-specifications, performance, production and conformity, NFP 18 470 2016, 2016.
[41] Association Francaise de Normalisation, National addition to Eurocode 2- Design of concrete structures: specific rules for ultra-high performance fibre-reinforced concrete (UHPFRC), NFP 18 710 2016, 2016.
[42] S. AFGC, Bétons fibrés à ultra-hautes performances–Recommandations, AFGC, Fr., 2013.
[43] The European Union Per Regulation 305/2011, D. 2004/18/EC Directive 98/34/EC, EN 1992–1-1: Eurocode 2: Design of concrete structures, Eur. Stand., 2004.
[44] S.I.A. CT, 2052: Béton fibré ultra-performant (BFUP)-Matériaux, dimensionnement et exécution, Zürich Société Suisse Des Ingénieurs Archit., 2015.
[45] S.S. Association, SIA 260: Basis of structural design, Swiss Soc. Eng. Archit. Zurich, Switz. (2003).
[46] E.J. Mezquida-Alcaraz, Numerical Modelling of UHPFRC: From the Material to the Structural Element, Univ. Politècnica València, València, 2021, https://doi.org/10.4995/Thesis/10251/167017 (PhD Thesis).
[47] E.J. Mezquida-Alcaraz, J. Navarro-Gregori, P. Serna-Ros, Direct procedure to characterize the tensile constitutive behavior of strain-softening and strain-hardening UHPFRC, Cem. Concr. Compos. 115 (2021), 103854, https://doi.org/10.1016/j.cemconcomp.2020.103854.
[48] E.J. Mezquida-Alcaraz, J. Navarro-Gregori, J.A. López, P. Serna-Ros, Validation of a non-linear hinge model for tensile behavior of UHPFRC using a Finite Element Model, Comput. Concr. 23 (2019) 11–23, https://doi.org/10.12989/cac.2019.23.1.011.
[49] J.Á. López, Characterisation of the Tensile Behaviour of UHPFRC by Means of Four-point Bending Tests, Univ. Politècnica València, València, 2017, https://doi.org/10.4995/Thesis/10251/79740 (PhD Thesis).

[50] J.Á. López, P. Serna, J. Navarro-Gregori, H. Coll, A simplified five-point inverse analysis method to determine the tensile properties of UHPFRC from unnotched four-point bending tests, Compos. Part B Eng. 91 (2016) 189–204, https://doi.org/10.1016/j.compositesb.2016.01.026.
[51] J. López, P. Serna, J. Navarro-Gregori, H. Coll, Characterisation of the strain-hardening behaviour of UHFPRC using the Third-Point-Bending Test, Proc. 4th HIPERMAT Int. Symp. UHPC. Kassel., 2016.
[52] ReSHEALience: Rethinking coastal defence and green Energy Service infrastructures through enHancEd durAbility high-performance fiber reinforced cement based materials., Funding from Eur. Union's Horiz. H2020 Res. Innov. Program. under Grant Agreem. No 760824, 2018-2021, n.d. ⟨https://uhdc.eu⟩.
[53] A. Tretjakov, S. Sideri, K. Nelson, E. Gastaldo, Recommendation on the use of crystalline admixtures, nanofibers, and nanocellulose for production of UHDC, ReSHEALience Proj. Public Deliv. D4.1 (2018). ⟨https://uhdc.eu/⟩.
[54] P. Serna, M. Roig-Flores, E.J. Mezquida-Alcaraz, A. Peled, O. Regev, L. Ferrara, F. Lo Monte, E. Cuenca, M. Reichardt, C. Schröfl, V. Mechtcherine, R.P. Borg, E. Camacho, J.Á. López, H. Coll, Guidelines for mix design formulation of functionalized UHDC and adaption to different application technologies, ReSHEALience Proj. Public Deliv. D4.2 (2019). ⟨https://uhdc.eu/⟩.
[55] J.A. López, P. Serna, J. Navarro-Gregori, Advances in the development of the first UHPFRC Recommendations in Spain: Material classification, design and characterization, in: F. Toutlemonde, J. ResplendinoT.Ch. (Eds.), UHPFRC 2017 Des. Build. with UHPFRC New Large-Scale Implementations, Recent Tech. Adv. Exp. Stand., RILEM Publications SARL, 2017, pp. 565–574.
[56] E.J. Mezquida-Alcaraz, J. Navarro-Gregori, P. Serna-Ros, Numerical validation of a simplified inverse analysis method to characterize the tensile properties in strain-softening UHPFRC, IOP Conf. Ser. Mater. Sci. Eng. (2019), https://doi.org/10.1088/1757-899X/596/1/012006.
[57] T. Leutbecher, Rissbildung und Zugtragverhalten von mit Stabstahl und Fasern bewehrtem ultrahochfesten Beton (UHPC), Kassel University Press GmbH, 2008.
[58] T. Pfyl, Tragverhalten von stahlfaserbeton, vdf Hochschulverlag AG, 2003.
[59] DIANA (Software), User's Manual – Release 10.2, TNO DIANA, Netherlands, 2017. ⟨https://dianafea.com/manuals/d102/Diana.html⟩.
[60] E.J. Mezquida-Alcaraz, J. Navarro-Gregori, J.A. López, P. Serna-Ros, Numerical Validation of a Simplified Inverse Analysis Method to Characterise the Tensile Behaviour of UHPFRC, in: FRC2018 Fibre Reinf. Concr. from Des. to Struct. Appl. Jt. ACI-Fib-RILEM Int. Work., 2018.
[61] P.H. Bischoff, Discussion of "Tension stiffening in lightly reinforced concrete slabs" by R. Ian Gilbert, J. Struct. Eng. 134 (2008) 1259–1260.